Astronomy & Astrophysics manuscript no. SXCS˙BrightSample˙final
July 24, 2014
© ESO 2014

arXiv:1405.3464v2 [astro-ph.CO] 23 Jul 2014

The Swift X-ray Telescope Cluster Survey. II. X-ray spectral analysis⋆,⋆⋆

P. Tozzi[1], A. Moretti[2], E. Tundo[1], T. Liu[3], P. Rosati[4], S. Borgani[5,6,7], G. Tagliaferri[8], S. Campana[8], D. Fugazza[8] , P. D'Avanzo[8]

[1] INAF, Osservatorio Astrofisico di Firenze, Largo Enrico Fermi 5, I-50125, Firenze, Italy
[2] INAF, Osservatorio Astronomico di Brera, via Brera 28, I-20121 Milano, Italy
[3] USTC, No.96, JinZhai Road Baohe District, Hefei, Anhui, 230026, P.R.China
[4] Università degli Studi di Ferrara, Dipartimento di Fisica e Scienze della Terra, Via Saragat 1 I-44121 Ferrara. Italy
[5] INAF, Osservatorio Astronomico di Trieste, via G. B. Tiepolo 11, I–34143, Trieste, Italy
[6] Dipartimento di Fisica dell'Università di Trieste, via G.B. Tiepolo 11, I–34131, Trieste, Italy
[7] INFN-National Institute for Nuclear Physics, via Valerio 2, I–34127, Trieste
[8] INAF, Osservatorio Astronomico di Brera, via Bianchi 46, I-23807, Merate (LC), Italy

Received 9 October 2013 / Accepted 16 May 2014

ABSTRACT

Aims. We present a spectral analysis of a new, flux-limited sample of 72 X-ray selected clusters of galaxies identified with the X-ray Telescope (XRT) on board the Swift satellite down to a flux limit of $\sim 10^{-14}$ erg s^{-1} cm^{-2} (SWXCS). We carry out a detailed X-ray spectral analysis with the twofold aim of measuring redshifts and characterizing the properties of the Intra-Cluster Medium (ICM) for the majority of the SWXCS sources.
Methods. Optical counterparts and spectroscopic or photometric redshifts for some of the sources are obtained with a cross-correlation with the NASA/IPAC Extragalactic Database. Additional photometric redshifts are computed with a dedicated follow-up program with the Telescopio Nazionale Galileo and a cross-correlation with the Sloan Digital Sky Survey. In addition, we also blindly search for the Hydrogen-like and He-like iron K_α emission line complex in the X-ray spectrum. We detect the iron emission lines in 35% of the sample, and hence obtain a robust measure of the X-ray redshift z_X with typical rms error 1 – 5%. We use z_X whenever the optical redshift is not available. Finally, for all the sources with measured redshift, background-subtracted spectra are fitted with a single-temperature `mekal` model to measure global temperature, X-ray luminosity and iron abundance of the ICM. We perform extensive spectral simulations to accounts for fitting bias, and to assess the robustness of our results. We derive a criterion to select reliable best-fit models and an empirical formula to account for fitting bias. The bias-corrected values are then used to investigate the scaling properties of the X-ray observables.
Results. Overall, we are able to characterize the ICM of 46 sources with redshifts (64% of the sample). The sample is mostly constituted by clusters with temperatures between 3 and 10 keV, plus 14 low-mass clusters and groups with temperatures below 3 keV. The redshift distribution peaks around $z \sim 0.25$ and extends up to $z \sim 1$, with 60% of the sample at $0.1 < z < 0.4$. We derive the Luminosity-Temperature relation for these 46 sources, finding good agreement with previous studies.
Conclusions. Thanks to the good X-ray spectral quality and the low background of Swift/XRT, we are able to measure ICM temperatures and X-ray luminosities for the 46 sources with redshifts. Once redshifts are available for the remaining 26 sources, this sample will constitute a well-characterized, flux-limited catalog of clusters distributed over a broad redshift range ($0.1 \le z \le 1.0$) providing a statistically complete view of the cluster population with a selection function that allows a proper treatment of any measurement bias. The quality of the SWXCS sample is comparable to other samples available in the literature and obtained with much larger X-ray telescopes. Our results have interesting implications for the design of future X-ray survey telescopes, characterized by good-quality PSF over the entire field of view and low background.

Key words. galaxies: clusters: general – galaxies: high-redshift – cosmology: observations – X-ray: galaxies: clusters – intergalactic medium

1. Introduction

Clusters of galaxies are at the crossroads of astrophysics and cosmology (see Kravtsov & Borgani 2012). Their baryon content is mostly in the form of a hot, diffuse plasma, the intracluster medium (ICM), which emits in the classic X-ray band 0.5 – 10 keV. In the last decade, observations with *Chandra* and XMM-Newton satellites revealed a wealth of complex phenomena going on in the ICM (see Markevitch & Vikhlinin 2007; McNamara & Nulsen 2007), and allowed to trace its chemical and thermodynamical evolution up to redshift $z \sim 1.3$ (see Ettori et al. 2004; Balestra et al. 2007; Maughan et al. 2008; Anderson et al. 2009). Despite the rich physics involved, the hydrostatic equilibrium is typically satisfied and robust mass proxies can be obtained by X-ray observations (see Kravtsov et al. 2006). This information, coupled with a well-defined selection function, allows one to compute the mass function of galaxy clusters over a broad range of redshifts. Ultimately, one can use X-ray selected cluster samples to constrain the cosmo-

⋆ Tables 1 and 2 and Appendix A are available in electronic form at http://www.anda.org
⋆⋆ Catalog and data products of SWXCS, constantly updated, are made available to the public through the websites http://www.arcetri.astro.it/SWXCS/ and http://swxcs.ustc.edu.cn/

logical parameters and the spectrum of the primordial density fluctuations (see Rosati et al. 2002; Schuecker 2005; Voit 2005; Borgani 2008; Vikhlinin et al. 2009; Mantz et al. 2010; Böhringer & Werner 2010; Allen et al. 2011). We note, however, that the main contribution of *Chandra* and XMM-Newton consists in providing the detailed properties of clusters already identified in previous X-ray missions.

The state–of–the–art of cosmological tests with clusters (Vikhlinin et al. 2009; Allen et al. 2011) has been obtained thanks to deep follow-up observations with *Chandra* of targets discovered in previous ROSAT wide-angle surveys or in ROSAT serendipitous fields. A key aspect is that the three major X-ray facilities existing today (*Chandra*, XMM–Newton and Suzaku) have a limited field of view ($\sim 0.1 - 0.2$ deg^2) and are mostly used in deep, targeted observations, which better fit their instrumental properties. In the case of *Chandra*, the process of assembling a wide and deep survey is slow due to the small field of view (FOV) and the low collecting area. On the other hand, its exquisite angular resolution ($\sim$ 1 arcsec at the aimpoint) makes it extremely easy to identify extended sources. In the case of XMM-Newton the collecting area is significantly higher, but the identification of extended sources, in particular at medium and high redshift, is more difficult due to the larger size of the Point Spread Function (PSF, whose half energy width is 15" at the aimpoint) and its rapid degradation as a function of the off–axis angle. In addition, the relatively high and unstable background may hamper the proper characterization of low surface-brightness sources. Finally, the large PSF of the X-ray Telescope on board Suzaku ($\sim$ 2 arcmin) makes it unfit to the detection of groups and clusters, despite its low background. An obvious strategy is to exploit the entire archive of these telescopes to identify serendipitously new X-ray cluster candidates. However, the discovery data of X-ray clusters, in general, are not sufficient to provide a reliable mass proxy, except for the brightest ones, and therefore a time–consuming follow-up is always needed in order to measure at least the global temperature from their ICM emission.

Despite these difficulties, several cluster surveys based on *Chandra* and XMM–Newton are currently ongoing. These surveys are based on the compilation of serendipitous medium and deep–exposure observations not associated to previously known X-ray clusters, or assembled with dedicated contiguous observations (Adami et al. 2011; Šuhada et al. 2012). An updated list of surveys as of mid-2012 is presented in Table 1 of Tundo et al. (2012). Some of these projects are aiming mostly at high redshift ($z > 1$) clusters (XDCP, Fassbender et al. 2011) thanks to the exploitation of the large number of archival extragalactic fields (i.e., avoiding the Galactic plane). Among these surveys, the largest solid angle covered with sparse fields is $\sim$ 400 deg ^{2} (XCS, Lloyd-Davies et al. 2011), and the maximum number of clusters candidates is $\sim$ 1000. However, the typical size of a complete and well defined cluster sample amounts at best to $\sim$ 100 objects, and, as already mentioned, in most cases X-ray data are not sufficient to properly characterize them (i.e., to have a robust mass proxy). In conclusion, the design of current large X-ray telescopes is optimized to obtain detailed images and/or spectra of isolated sources to explore the deep X-ray sky, while they are not efficient as survey instruments. Therefore, a substantially different mission strategy is required for surveys.

Looking at the near future, the planned eROSITA satellite (Predehl et al. 2010; Merloni et al. 2012), will finally provide a long-awaited all-sky survey at a depth more than one order of magnitude larger than the ROSAT All-Sky Survey. However, due to its low angular resolution the eROSITA discovery space is limited for distant clusters. In particular, the X-ray telescope hits the confusion limit at fluxes $\sim 10^{-14}$ erg s^{-1} cm^{-2}, and, as a consequence, the cluster selection function will rapidly drop at high redshifts. In addition, the low effective area above 2 keV severely limits the characterization of the ICM in medium and high temperature clusters (Borm et al. 2014).

The urge of a wide and deep all-sky survey in the X-ray band for clusters is even stronger if we consider what is happening at other wavelengths. In particular, Sunyaev-Zeldovich (SZ) surveys of clusters are providing the first exciting results. Recent results from the South Pole Telescope Survey (Reichardt et al. 2013) and the Atacama Cosmology Project (Sehgal et al. 2011) showed that SZ selection is efficient and can identify clusters up to high redshift. Recently, the all-sky survey of the Planck satellite provided a cluster catalog of about 1200 SZ-selected clusters (Planck Collaboration et al. 2013a). Cosmological constraints from the SZ, all-sky Planck survey are found to depend mostly on possible systematic bias in the relation between the total mass and the SZ parameter Y (Planck Collaboration et al. 2013c). Indeed, the X-ray follow–up of SZ clusters is crucial to fully exploit the cosmological relevance of SZ surveys, either for narrowing down the uncertainties on the cluster mass, or to firmly evaluate purity and completeness of the sample. However, in the future, SZ cluster surveys are expected to dominate the field of ICM physics and cosmological tests with clusters of galaxies. Only a survey-optimized mission like the proposed Wide Field X-ray Telescope (WFXT, Murray et al. 2010; Rosati et al. 2011) can provide a large number of new detections well below the 10^{-14} erg s^{-1} cm^{-2} flux limit, therefore entering the unexplored realm of distant X-ray clusters, and, at the same time, provide X-ray mass proxies and redshifts for a large number of them. We also stress that the combination of future SZ surveys and deep, wide-angle X-ray surveys is the unique way to take full advantage of galaxy clusters as tracers of the growth of cosmic structures. To summarize, a wide-field, sensitive, X-ray mission will be the only means to bring our view of the X-ray sky, in terms of solid angle and sensitivity, at the level of the surveys in other wavelengths as planned in the next decade.

In this framework, we are undertaking a new cluster survey using an X-ray facility that was never exploited before for this goal: the X-ray Telescope (XRT) on board the Swift satellite (Burrows et al. 2005). Despite its low collecting area (about one fifth of that of *Chandra* at 1 keV), XRT has characteristics which are optimal for X-ray cluster surveys: a low background, an almost constant PSF across the FOV (Moretti et al. 2007) and spectral capability up to 7 keV. Moreover, almost all the Swift/XRT pointings can be used to build a serendipitous survey based on the follow-up fields centered on Gamma Ray Bursts (GRB) detected by Swift. The *Swift-XRT cluster survey* (SWXCS) has a sky coverage ranging from total 40 deg^2 to 1 deg^2 at a flux limit of about 10^{-14} erg s^{-1} cm^{-2}. The first catalog, including 72 sources, has been published in Tundo et al. (2012), hereafter Paper I. The SWXCS has been realized using 336 fields with galactic latitude $|b| > 20^\circ$ centered on GRBs present in the XRT archive as of April 2010. This catalog is already one of the deepest samples of X-ray selected clusters, with a well defined completeness criterion and a negligible contamination. The SWXCS sample is expected to grow by a factor of at least $\sim$ 3 in the eventual analysis of the full Swift/XRT archive, which will be based on a newly developed detection strategy (Liu et al. 2013).

In this Paper we perform the X-ray spectral analysis of the 72 sources in the SWXCS catalog of Paper I to measure their temperature, total luminosity, metal abundance and

redshift. The paper is organized as follows. In Section 2 we briefly recall the properties of the XRT instrument, the X-ray data reduction procedure and the properties of the survey. In Section 3 we collect the redshift for the sources identified in the NASA Extragalactic Database (NED) and in the SLOAN Digital Sky Survey (SDSS), and present new photometric redshifts for some of our sources from a dedicated optical follow-up with the Telescopio Nazionale Galileo (TNG). In Section 4 we present and discuss our X-ray spectral analysis for all the sources with redshift information. In Section 5 we present the X-ray spectral analysis of a serendipitous *Chandra* observation of one SWXCS source, providing a simple but revealing comparison of the two instruments. Finally, in Section 6, we summarize our results and discuss them in the context of present and future X-ray cluster studies. We assume the 9-year WMAP cosmological parameter results: $H_0 = 69.7$ km/s/Mpc, $\Omega_m = 0.28$, $\Omega_\Lambda = 0.72$ (see Hinshaw et al. 2013). Our results are clearly unaffected by the most recent *Planck* cosmological results (Planck Collaboration et al. 2013b).

2. Instrument, data reduction and survey properties

In this Section we briefly recall the properties of the XRT instruments, the data reduction, and the main characteristics of the SWXCS sample. For more details we refer to Paper I.

2.1. The X-ray Telescope

The XRT is part of the scientific payload of the Swift satellite (Gehrels et al. 2004), a mission dedicated to the study of gamma-ray bursts (GRBs) and their afterglows operating since November 2004. GRBs are detected and localized by the Burst Alert Telescope (BAT, Barthelmy et al. 2005), in the 15 – 300 keV energy band and followed-up at X-ray energies (0.3 – 10 keV) by the X-Ray Telescope (XRT). The XRT (Burrows et al. 2005) is an X-ray CCD imaging spectrometer which utilizes the third flight mirror module originally developed for the JET-X telescope (Citterio et al. 1994) to focus X-rays onto a XMM-Newton/EPIC MOS CCD detector (Burrows et al. 2005). The effective FOV of the system is ∼ 24 arcmin. The PSF, similar to XMM-Newton, is characterized by a half energy width (HEW) of ∼ 18 arcsec at 1.5 keV (Moretti et al. 2007) and, most important, is almost flat across the entire FOV, with a negligible dependence on the photon energy. Finally, XRT has the lowest background not associated to astronomical sources among the currently operating X-ray telescopes due to the low orbit and its short focal length. This aspect has been recently exploited to make an unprecedented measure of the residual hard (2–10 keV) X-ray background, thanks to a combination of deep Chandra and XRT data (Moretti et al. 2012). Clearly, the low X-ray background has a strongly positive impact on the detection of extended sources at all fluxes. In Figure 2 of Moretti et al. (2012) we show that the ratio signal/background for extended sources is a factor ∼ 10 better in Swift-XRT than in *Chandra*.

2.2. Data reduction and analysis

In Paper I we considered the Swift/XRT archive from February 2005 to April 2010, including 336 fields in the corresponding GRB positions, with Galactic latitude $|b| > 20°$, to avoid crowded fields and strong Galactic absorption. We followed a standard data reduction procedure by means of the `xrtpipeline` task of the current release of the HEADAS software (version v6.8) with the most updated calibration (CALDB version 20111031, Nov 2011). Then, we proceeded with a customized data reduction, aimed at optimizing our data to the detection of extended sources. The most important aspect of this step is the reduction of the background thanks to the exclusion of the intense GRB emission at the beginning of each observation, after a careful investigation of the background light curves.

The identification of the X-ray sources is performed with the standard algorithm `wavdetect` within the CIAO software used successfully on *Chandra* and XMM-Newton images (Lloyd-Davies et al. 2011). We run the algorithm on the images obtained in the soft (0.5 – 2 keV) band. This step leads us to identify a total of $\sim 10^4$ sources in the 336 GRB fields. Among them, we select extended sources with a simple criterion based on the measured Half Power Radius (HPR) effectively defined as the 50% encircled energy radius within a box of 45×45 arcsec, which includes 80% of the flux of a point source. The choice of a restricted region is motivated by the need of sampling the growth curve with a high signal-to-noise ratio (S/N).

Extensive simulations spanning all the parameter range found in the survey (in particular source fluxes and background levels) have been used to estimate the expected distribution of the HPR for point sources. The simulations allow us to identify a threshold values HPR_{th} above which a source is inconsistent with being unresolved at the 99% level. This criterion does not depend on the off–axis angle θ, but significantly depends on the image background. The expected number of spurious sources in the entire survey surviving this criterion is ∼ 5. Finally, our sample is constituted by all the sources satisfying our criteria with more than 100 net counts in the soft band within the extraction radius R_{ext} (defined by the circular region where the source surface brightness is larger than the background level). In addition, the low number of sources in the final list allows us to perform a careful visual inspection of each source candidate, hence significantly reducing the number of spurious detections.

The sky coverage ranges from 40 deg^2 at the high-flux end, to 1 deg^2 at 10^{-14} erg s^{-1} cm^{-2} (the flux limit of the survey). The sky coverage is comparable to that of RDCS by Rosati et al. (1998), while it is lower but deeper than that of the 400sd survey by Burenin et al. (2007), as shown in Figure 13 of Paper I. We also characterize the completeness of the sample, defined as the fraction of extended sources actually selected as extended by our procedure as a function of their soft-band net counts. In order to do that, we produce another set of simulations with a few thousand extended sources, modeled from ten real cluster images originally obtained with the *Chandra* satellite (therefore with a resolution much higher that that of XRT), cloned at a typical redshift and re sampled at the XRT resolution. This cloning procedure, already used to investigate the evolution of cool core clusters at high redshift (see Santos et al. 2008, 2010) allows us to measure the completeness of the sample in the assumption that the cluster images used for cloning are representative of the entire cluster population. We find that the completeness is a function of the input counts, starting from ∼70% for sources just above our threshold of ∼100 net counts within the extraction regions. This level increases to ∼90% for sources with ∼200 net counts, and reaches a completeness level >95% for sources with ∼300 net counts (see Figure 9 of Paper I). Given the distribution of exposure times and the observed logN-logS of groups and clusters, this implies that we may have missed, in total, about 10 extended sources, mostly with less than 200 counts, above the nominal flux limits associated to each field. From simulations, it appears that the major source of incompleteness is due to the blending of bright, unresolved sources.

2.3. The Swift-X-ray Cluster Survey: the GRB fields

Our final catalog consists of 72 X-ray extended sources detected with ≥ 100 soft net counts. The measured net counts from each source are computed by aperture photometry within the extraction radius R_{ext}, after removing the emission associated to point sources included in this region. The net count rate measured for each source is obtained dividing the net counts by the exposure time, after correcting for vignetting effects in the soft band. From the corrected net count rate, the energy flux is computed simply by multiplying it by the energy conversion factor (ECF) computed at the aimpoint, whose value for a thermal spectrum is typically 2.35×10^{-11} erg s^{-1} cm^{-2}/ (cts s^{-1}), with a maximum systematic uncertainty of 0.1×10^{-11} erg s^{-1} cm^{-2}/ (cts s^{-1}). This value has a weak dependence on the ICM temperature and the redshift, and a significant dependence on the Galactic absorption. The effect of Galactic absorption in each source position is taken into account assuming the Galactic N_H values measured in the radio survey in the Leiden/Argentine/Bonn survey (Kalberla et al. 2005). Finally, the total net flux is obtained by accounting for the missed contribution beyond R_{ext}. In order to measure the lost signal, we fit the surface brightness (*SB*) of every extended source with a King profile. Then, we extend the surface brightness profile up to $2 \times R_{ext}$. The photometric properties of the SWXCS sources are published in Paper I, along with a preliminary optical identification for some of the sources obtained with a simple cross-correlation with the NED database. In this paper, the energy fluxes obtained fitting the X-ray spectra will supersede the fluxes obtained with the ECFs.

3. Redshift from optical counterparts

We collect the redshifts for our sources as follows. First we retrieve the spectroscopic or photometric redshift from the literature, using the NASA Extragalactic Database (NED); then we compute the photometric redshift for 12 sources imaged by the TNG with a dedicated program. Eventually, we use the optical redshift (both spectroscopic and photometric) to assess the robustness of the redshift z_X measured by the X-ray spectral analysis through the identification of the K_α iron line complex. This allows us to assess the reliability of X-ray redshift measurements for sources without optical redshift. In this section, we present and discuss the optical redshifts.

3.1. Cross correlation with optical catalogs

A preliminary identification with optical counterparts in NED has been performed in Paper I (see their Table 3). Here we briefly describe the adopted procedure and the results, updating in few cases the results of Paper I.

First we checked for counterparts in optical cluster surveys, assuming a search radius of 1 arcmin from our X-ray centroid. The choice of 1 arcmin is motivated by the following facts. The X-ray centroid of SWXCS sources is measured with an accuracy of about ≤ 7 arcsec, depending on the S/N of the source and the surface brightness distribution. We expect that the X-ray emission is often peaked close to the central galaxy, even in the absence of a cool core, while a significant displacement of the X-ray centroid with respect to the brightest galaxy (i.e., several tens of arcsec) is expected only in the rare occurrence of ongoing massive mergers. We are also aware that the position of optically selected clusters could be uncertain up to 1 arcmin, or even more in the case of sparse optical clusters. Given that 1 arcmin corresponds to 200 kpc at the typical redshift of 0.2, and considering the strong dependence of the galaxy density from radius in clusters, we argue that for the optical counterparts of our clusters, the uncertainty on the center is always below 1 arcmin. However, in order to include particular cases such as loose groups or strongly sub-structured clusters, we also search for counterparts up to 3 arcmin from our X-ray centroid. For all our source, we did not find any convincing candidates besides those closer than 1 arcmin.

We find a total of nineteen previously known, optically identified clusters with measured redshift, many of them listed in more than one catalog. Among them, nine are found in the Wen+Han+Liu cluster sample (WHL, Wen et al. 2009, 2012), which is an optical catalog of galaxy clusters obtained from an adaptive matched filter finder applied to Sloan Digital Sky Survey DR6. We report five clusters from the Gaussian Mixture Brightest Cluster Galaxy (GMBCG, Hao et al. 2010) based on SDSS DR7, which is an extension of the maxBCG cluster catalog (Koester et al. 2007) to redshift beyond 0.3 and on a slightly larger sky area $\sim$ 8000 deg^2 (one of these clusters is also in the MaxBCG catalog). We also find four clusters in the Abell catalogs (Abell et al. 1989), among them Abell 2141 which has been already studied in detail by Moretti et al. (2011) using XRT data. We also find one cluster in each of the following catalogs: the Northern Sky optical Cluster Survey (NSCS, Gal et al. 2003; Lopes et al. 2004), the Zwicky Cluster Catalog (CGCG, Zwicky et al. 1963), the Sloan Digital Sky Survey C4 Cluster Catalog (SDSS-C4-DR3, based on DR3, Miller et al. 2005; von der Linden et al. 2007), the Edinburgh-Durham Southern Galaxy Catalogue (EDCC, Lumsden et al. 1992), and the ESO/Uppsala Survey of the ESO(B) Atlas (Lauberts 1982). Finally, we find four clusters in the Szabo et al. (2011) catalog (AMF clusters) which is also based on an adaptive matched filter finder applied to Sloan Digital Sky Survey DR6, but it is not included in the NED. One of the four AMF clusters is not included in any of the previous catalogs found in the NED. Note that we removed the optical identification of SWXCS J232248+0548.1 reported in Paper I with the NSCS cluster at $z_{phot} = 0.45$, whose distance from the centroid is ~ 1 arcmin, since our new photo-z and z_X both indicates a lower value (see Section 4).

To increase the number of available redshifts, we also search for galaxies with published redshift not associated to previously known clusters within a search radius of 7 arcsec from the X-ray centroid of our sources. We find 11 galaxies, whose redshift is always consistent with the photometric redshift of the optical cluster counterpart when present. This finding shows that our matching criterion is efficient in identifying the central cluster galaxy. Therefore, in the 4 cases where no optical cluster counterpart is found, we assign the galaxy redshift to our X-ray source.

To summarize, we have 23 optical redshifts (spectroscopic or photometric) published in the literature and associated to our cluster candidates. Whenever a photometric redshift and the spectroscopic redshift are both present, we use the spectroscopic one. The redshifts obtained from the literature are reported in the second column of Table 1. This table is consistent with its preliminary version presented in Paper I except for the removed identification of SWXCS J232248+0548.1, and two identifications with Abell clusters previously missed.

We also remark that we now use the new designation "SWXCS J" for our clusters, as opposed to "SWJ" used in Paper I. This new acronym has been officially accepted by the IAU Registry of a new acronym in February 2013. The format is SWXCS JHHMMSS+DDMM.m. For clarity, we add, in the last column of Table 1, the name used in Paper I.

3.2. Redshift from optical follow-up with TNG

For twelve clusters we obtained photometric redshifts with a dedicated program at the TNG (AOT 22, PI A. Moretti). Our strategy consisted in supplementing SDSS data with NICS *J* and DOLORES *r* deep observations (20 minutes each filter) when SDSS data do not provide a clear counterpart (4 cases, plus 1 redundant). In the regions not covered by the SDSS we performed observations in the NICS *J* and DOLORES *r* g bands (7 cases). In all cases we performed the photometry of the brightest galaxy by means of SExtractor (Bertin & Arnouts 1996). We measured the photometric redshifts by means of the HYPERZ software (Bolzonella et al. 2000) using galaxy templates which are built with the spectrophotometric code of Bruzual & Charlot (2003), assuming exponentially declining star formation histories with time scales 0.5 Gyr, Chabrier IMF and metallicity 0.5 solar. We verified that varying the metallicity content and the age of the input template has a negligible impact on the redshift. We typically obtain a 1 σ error of about 10% on the photometric redshift. The photometric redshift obtained by our TNG follow-up are listed in the third column of Table 1.

We also explored the possibility of obtaining photometric redshifts from VLT imaging of the GRB fields. We note that, although most of the GRB have been followed up by VLT and other optical/IR telescopes, in most cases the X-ray centroids of our serendipitous sources fall outside the optical field of view. In only one case SWXCS J232345-3130.8, we are able to use the VLT optical/IR follow-up observation of GRB051001. We apply our photometric redshift measurement to this cluster which turns out to be the most distant in our subsample ($z = 0.85^{+0.07}_{-0.03}$).

To summarize, we have thirteen photometric redshifts which complement the information obtained by a cross-correlation with NED. One of them (SWXCS J084749+1331.7) already had a consistent spectroscopic z_{opt}. Therefore, a total of 35 sources, about half the total X-ray sample, have at least one optical measurement of the redshift.

4. Redshift from X-ray spectral analysis

The results from the X-ray spectral analysis will be provided only for the clusters with a robust redshift measurement, either from the optical or from the X-ray data. Therefore, first we blindly search for the iron K_α line complex in order to measure the X-ray redshift z_X in all cases where the S/N ratio allows us to do so. The measurement of X-ray redshift from *Chandra* data has been extensively explored by Yu et al. (2011). However, in the case of XRT we have a significantly different situation, due to the harder effective area of XRT with respect to that of *Chandra*, and to the typically lower S/N of our sources. Therefore, we cannot directly apply the criteria found in Yu et al. (2011) to our sample.

To exploit at best the information contained in our X-ray spectra, we proceed in two steps. First, we fit blindly all our X-ray spectra with a `mekal` model, leaving all relevant parameters, including the redshift, free to vary during the minimization procedure. Then, we compare the optical and X-ray redshifts for the sources which have both, to establish a new robust criterion to measure the redshift. Finally, we apply this criterion to the other sources with no optical redshift to obtain reliable z_X measurements.

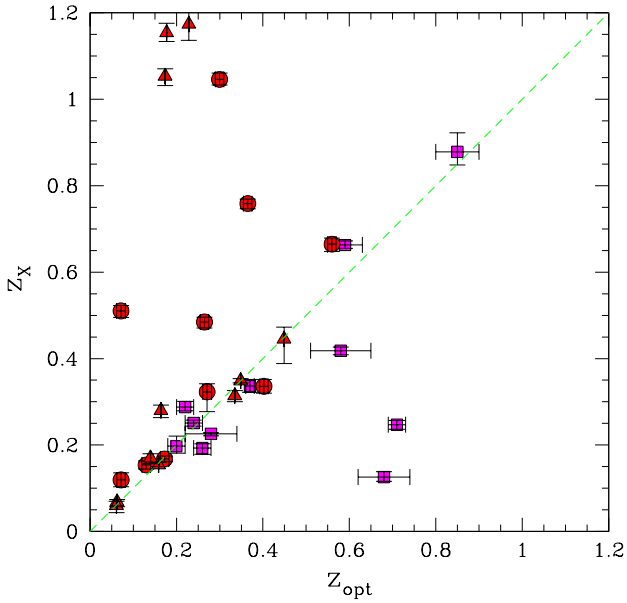

Fig. 1: X-ray vs. optical redshift for the 35 sources with spectroscopic or photometric redshift (three sources do not appear since they have $z_X > 1.2$). Red symbols are for clusters whose redshift is found in the literature after inspecting the NED database (circles and triangles are for photometric and spectroscopic redshifts, respectively). Magenta squares are for clusters whose photometric redshift has been computed by us with a dedicated TNG program or with VLT archive images (one case). Error bars on z_X and z_{opt} correspond to 1 σ.

4.1. Method

The spectra are extracted from circular regions with radius R_{ext}, defined as the radius where the surface brightness is equal to the background intensity. Intervening point sources are removed. We sampled the background from the same observation, in a region typically three times larger by size than the extraction region of the source spectra. Calibration files (rmf and arf) are built for each extraction region.

The background subtracted spectra are analyzed with *XSPEC* v.12.3.0 (Arnaud 1996). We use the *C-statistic* to find the best-fit parameters for the adopted model (see Bevington & Robinson 2003; Arnaud et al. 2011). The Cash statistic parameter C_{stat} (Cash 1979) provides a better criterion with respect to the canonical χ^2 analysis of binned data, particularly for low S/N spectra (Nousek & Shue 1989). However, we first apply a `group min 1` command in `GRPPHA`, to have at least 1 count per bin. This step is necessary for *XSPEC* to correctly calculate the *C-statistic* (Arnaud, private communication; see also Evans et al. (2009)). All our sources are fitted with a single temperature `mekal` model (Kaastra 1992; Liedahl et al. 1995). The ratio between the elements are fixed to the solar values as in Asplund et al. (2005). We model the Galactic absorption with `tbabs` (Wilms et al. 2000) fixing the Galactic neutral Hydrogen column density to the values measured in the Leiden/Argentine/Bonn radio survey (Kalberla et al. 2005).

The fits were performed over the energy range 0.5-7.0 keV. We do not include photons with energies below 0.5 keV in order to avoid uncertainties due to a rapidly increasing background

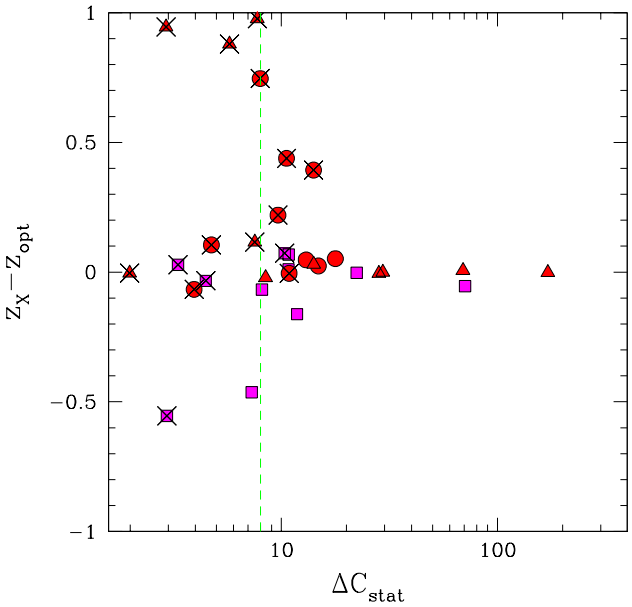

Fig. 2: Difference $z_X - z_{opt}$ for the 35 sources with spectroscopic or photometric redshift plotted as a function of the ΔC_{stat} value. Red circles (triangles) are for clusters whose photometric (spectroscopic) redshift is found in the literature through a match with the NED, while the magenta squares are for clusters whose photometric redshift has been computed by us with a dedicated TNG program or with VLT archival image (in one case). Crosses corresponds to z_X values rejected after a visual inspection because a secondary minimum in C_{stat} is found close to the minimum (see text for details). Error bars on z_X and z_{opt} correspond to 1 σ.

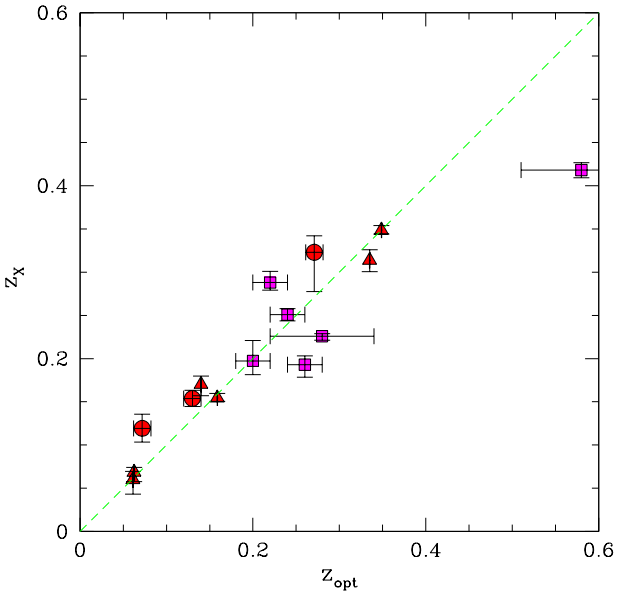

Fig. 3: X-ray vs. optical redshift for the 15 sources with spectroscopic or photometric redshift and X-ray redshift satisfying the selection criteria. Red circles (triangles) are for clusters whose photometric (spectroscopic) optical redshift is found in the literature through a match with the NED, while the magenta squares are for clusters whose photometric optical redshift has been computed by us with a dedicated TNG program or with VLT archival image (in one case). Error bars on z_X and z_{opt} correspond to 1 σ.

below 0.5 keV. The cut at high energies, instead, is imposed by the rapidly decreasing S/N, due to the combination of the lower effective area of XRT and of the exponential cut-off of the thermal spectra. With this choice we also avoid the strong calibration lines present in the XRT background.

4.2. Measurement of z_X

In the first step, we focus only on the presence of the K_α iron line complex and therefore on the best–fit redshift z_X. We fit the background-subtracted X-ray spectra assuming a `mekal` model, with N_H frozen to the Galactic value, while the redshift, metallicity, temperature and normalization parameters are left free. Once the best fit is found, we freeze the metallicity and temperature parameters and vary the redshift parameter only. Then, we plot the C_{stat} value as a function of the redshift and look for its minimum.

In Figure 1 we plot the comparison of z_X with z_{opt} for the 35 sources with photometric or spectroscopic optical redshift. While a large fraction of the z_X values are consistent with the optical redshift, there is a significant number of catastrophic failures. Therefore we need to apply a filter to select reliable measurements of z_X. To do that, first we find the absolute minimum in the parameter C_{stat}, then we explore the redshift space with the `steppar` command, covering the entire range of possible values from $z = 0$ to $z = 2$ with a very small step $\delta z = 0.01$. We then plot the difference ΔC_{stat} of the C_{stat} value with respect to the minimum as a function of redshift. In Yu et al. (2011) we investigated *Chandra* data to set a first criterion on the $C - statistic$ value $\Delta C_{stat} > 9$, corresponding to a confidence level of 3 σ as tested *a posteriori* with simulations. However, we also find that this criterion is not sufficient for sources with a low number of net detected counts. In particular, below 1000 total net counts (in the useful 0.5-7 keV band) the number of catastrophic failures rapidly increases, irrespective of ΔC_{stat}. Since most of the SWXCS sources have less than 1000 total net counts, we should reject the large majority of z_X measurements. On the other hand, from Figure 1 we find that, given the large fraction of the z_X measurements found to be in good agreement with the optical one, we can relax the criteria in order to include most of the low S/N XRT spectra. This is possible thanks to the larger ratio of the hard to soft effective area of XRT with respect to that of *Chandra*, as shown in Figure 1 in Paper I. This property implies that, for the same total number of net counts, a larger number of iron-line photons are found in XRT spectra than in *Chandra* spectra.

An obvious solution is simply to adopt a much larger ΔC_{stat} irrespective of the net counts. However, we still find catastrophic failures with ΔC_{stat} as high as 14. This would strongly limit the number of new z_X that we can measure for the remaining 37 sources with no optical redshift. Therefore we consider a different strategy based on a visual inspection of the ΔC_{stat} plots. We realize that additional information can be provided by the secondary minima in the ΔC_{stat} vs. z_X plots: whenever a significant number of secondary minima with a depth close to the principal minimum is found, we reject the z_X measurement. We find that a good choice is to require that the difference in ΔC_{stat} from the

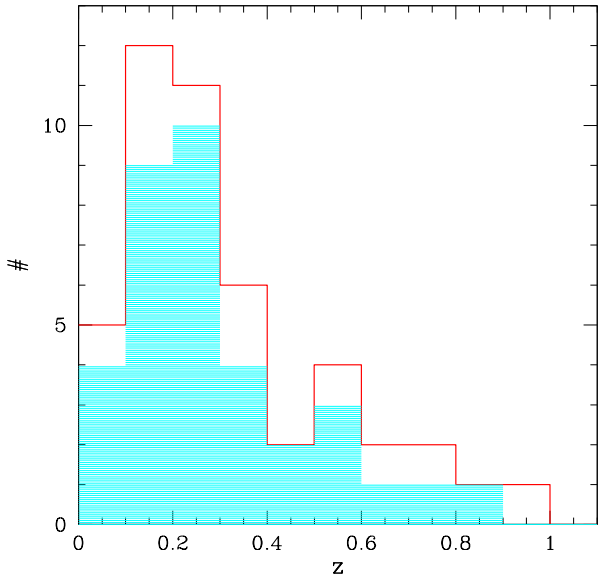

Fig. 4: Redshift histogram of the 46 clusters with redshift values with the following priority: i) optical spectroscopic redshift; ii) optical photometric redshift; iii) X-ray spectroscopic redshift. The shaded area corresponds to optical redshifts only (both spectroscopic and photometric).

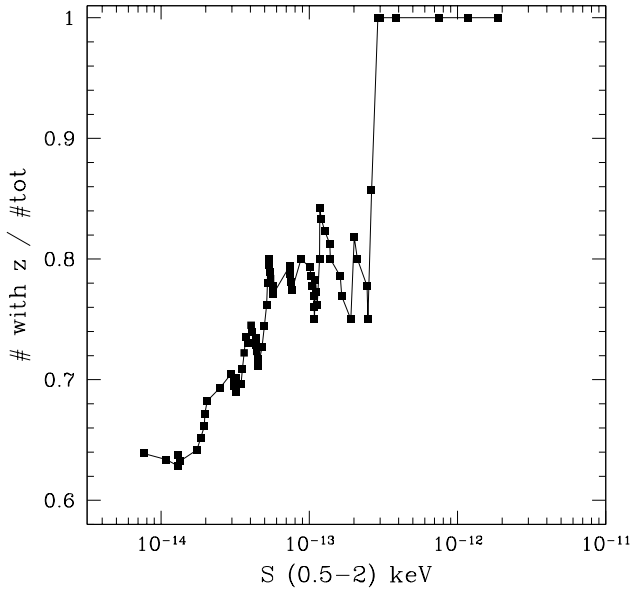

Fig. 5: Redshift completeness (defined as the ratio of sources with redshift over the total number of sources above a given flux) as a function of the energy flux in the soft band.

second deepest minimum must be larger than 2, irrespective of the ΔC_{stat} value of the absolute minimum. In Figure 2 we show the $\delta z = z_X - z_{opt}$ vs. ΔC_{stat}, where we marked with crosses the z_X measurements which do not fulfill the requirement on the secondary minima. We find that, after applying this filter, we find a reasonable agreement between z_X and z_{opt} for $\Delta C_{stat} > 8$, irrespective of the total net counts of the source. The z_{opt}-z_X relation for the 15 spectra satisfying the selection criteria is finally shown in Figure 3. We note that the discrepancy is often larger than expected on the basis of the formal 1 σ error bars on z_X. The largest discrepancy is for SWXCS J0926.0+3013.8 at $z_{opt} = 0.58 \pm 0.07$, which has, however, the largest uncertainty on the optical redshift. We postpone a more accurate investigation of the optimal criteria to measure z_X to the final SWXCS catalog, when a larger source statistics will allow us to refine our strategy (Liu et al. in preparation).

When we apply this criteria ($\Delta C_{stat} > 8$ and no secondary minima within $\Delta C_{stat} = 2$) to the rest of the sample, we are able to assign the redshift z_X to 11 sources without optical redshift. The 26 z_X values satisfying our criteria are listed in the fourth column of Table 1. The total number of sources with redshift is therefore 46. We use the redshift values with the following priority: i) optical spectroscopic redshift; ii) optical photometric redshift; iii) X-ray spectroscopic redshift. The histogram distribution of the redshifts in our sample is shown in Figure 4. The distribution has a strong peak around $z \sim 0.2$, while about 1/4 of the sources are at $z > 0.4$. We note that X-ray redshift measurements contribute mostly at high redshift. This is expected, since at higher redshift the Fe K_α line complex shift towards lower energies in the observing frame, where the effective area of XRT is larger.

4.3. Redshift completeness

We obtain the redshift information for 64% of the sample. Given the mixed criteria used to assign the redshift, we do not expect that the sources with redshift correspond to the bright end of the sample. In addition, since our detection criteria is based on the soft net counts, and since the exposure times are distributed on a broad range, we find that several X-ray bright sources still do not have X-ray redshift measurement. The redshift completeness, defined as the ratio of the number of sources with redshift to the total number of sources at fluxes larger than a given values, is shown in Figure 5.

We notice that the redshift completeness is not larger than 80% for fluxes below 3×10^{-13} erg s^{-1} cm^{-2}. This implies that if we want to extract a flux limited sample with a significant number of sources out of the total sample, either we are limited to few very bright sources, or we suffer a 20% incompleteness [1] Therefore, we conclude that a further effort to collect more redshifts must be done before this sample can be used to investigate the evolution of the X-ray properties, and, in the end, the mass function and the associated cosmological constraints. In the rest of the paper we present and discuss the properties of the clusters with redshift.

5. Spectral simulations and robustness of spectral fits

Before proceeding with the X-ray spectral analysis on the entire sample, and investigate scaling relations between observables, we thoroughly explore possible systematic uncertainties in our

[1] We also remind that this sample originally suffers from another source of incompleteness due to the X-ray selection process itself. The number of sources possibly missed by our X-ray selection has been estimated with extensive simulations as described in Paper I, and it can reach about 15% of the total sample (about ten sources).

best-fit temperature and abundance values associated to the fitting procedure. This step is particularly relevant given the low S/N regime of our spectra.

As a first check, we repeat all our fits adopting the χ^2 statistics and a binning of 20 counts per bin. This choice has a significant impact on the best fit values, since, given the low amount of counts, the binning has the effect of smoothing the spectra. We find a good agreement between the best-fit values of the temperatures obtained with the two methods, and also confirm that all the fits have an acceptable reduced χ^2 (on average $\langle\tilde{\chi}^2\rangle \sim 1.07$). However, we also find that, on average, the best-fit values obtained with the χ^2 are 8% lower than those obtained with the Cash statistics. This can be visually appreciated in Figure 6. We note that Branchesi et al. (2007a) also found larger temperatures with Cash statistics with respect to χ^2, but by a much smaller amounts $\sim$ 1%. However, their results are not directly comparable to ours given the different instrument (*Chandra*) and the different S/N regime. On the other hand, the best-fit values of Z_{Fe} obtained with the χ^2 is significantly larger than those obtained with the Cash statistics. This is not surprising, since the binning washes out the emission line features, hampering also the measurement of z_X. As a further check, we also repeat our fit assuming an `apec` model instead of the `mekal` model, and we find no differences in the temperature best-fit values, while Z_{Fe} values are lower by 20% on average. Since the detection of the Fe emission line is a key step in our strategy, we keep using the Cash statistics with a `mekal` model in our analysis.

Then, we assess the robustness of our best-fit temperature values. First, we notice that in our sample we have only 5 sources whose spectrum has more than 1500 counts in the total 0.5-7 keV band[2], which is traditionally considered a safe lower limit for spectral analysis. Moreover, we have 30 sources whose spectra have $100 < Cts < 500$, a regime which is usually not considered reliable for spectral analysis. Therefore, we carefully investigate the performance of our spectral fitting strategy in this regime by extensive spectral simulations.

We set up our simulations in order to reproduce at best the characteristics of the SWXCS, with a particular focus on the measurement of the average temperature. The parameters which can in principle affect the accuracy of the temperature measurements for a given number of net detected counts are: redshift, the temperature itself, the iron abundance, the Galactic absorption, the position on the detector, the size of the source and the exposure time (and hence the background level in the source region). Clearly, the entire parameter space is too large to be fully investigated. Therefore we choose a typical situation for our survey, consisting in an exposure time of 150 ks (see Figure 5 in Paper I) and a circular extraction region with a radius of 1.7 arcmin, with average response matrix files. The source size and the chosen exposure time set the intensity of the background, which is sampled from real XRT data with no source included. The background level in each source spectrum typically amounts to about 300 net counts in the 0.5-7 keV band, and it is re-simulated for each spectrum. We also set a typical redshift of $\langle z\rangle = 0.25$ (see Figure 4) and a typical Galactic absorption $N_{Hgal} = 2{\times}10^{20}$ cm^{-2} (see Figure 12 in Paper I). We vary the normalization of the input spectrum in order to have, on average, 1700, 1000, 750, 500, 300, 200, 150 and 100 net counts in the 0.5-7 keV band. We adopt the same fitting strategy (with a fixed redshift and a free abundance parameter) and compare the recovered best-fit temperature and iron abundance with the input values. Each parameter set is simulated 1000 times.

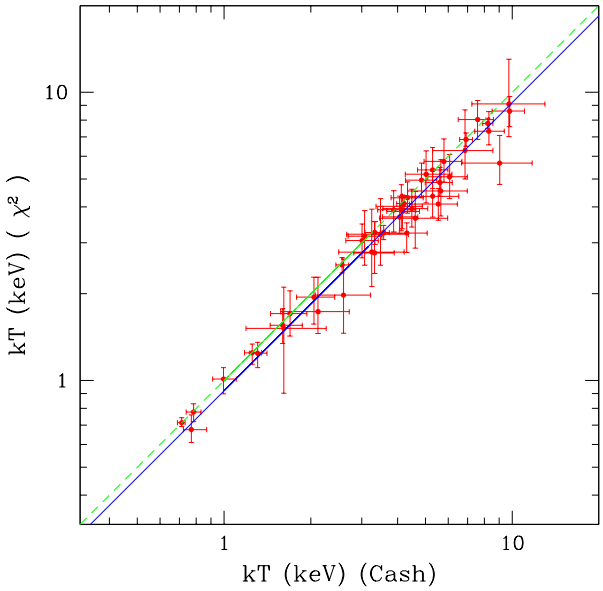

Fig. 6: Best-fit temperatures values obtained with χ^2 vs those obtained with our reference analysis using Cash-statistics. The dashed line shows the $kT_{\chi^2} = kT_{Cstat}$ relation, while the solid line shows the $kT_{\chi^2} = 0.925 \times kT_{Cstat}$ relation.

In Figure 7 we show the ratio of the best-fit temperature to the input value as a function of the net detected counts, for four representative input temperatures (7.5, 5, 3 and 1.5 keV). These simulation set is the best compromise to cover at best the parameter space of our data set. Each point in Figure 7 represents the ratio $kT_{best-fit}/kT_{input}$ averaged over 1000 realizations, while the error bars represent the 1 σ rms on the mean. We can express the average best-fit temperature as a function of the true (input) temperature and the net detected counts as $kT_{best-fit} = R(kT_{input,Cts}) \times T_{input}$. With a simple minimization procedure, we find that the best approximation for the function $R(kT_{input,Cts})$ is

$$R(kT_{input}, Cts) = 1{+}0.01{\times}\Big(\frac{kT_{inut}}{5}\Big)^{0.39}{+}1.45{\times}\Big(\frac{kT_{input}}{5}\Big)^{1.5}{\times}\Big(\frac{Cts}{100}\Big)^{-2.0} \quad (1)$$

We find $\langle T_{best}\rangle/T_{input} \leq 1.10$ when the net counts are above 500 irrespective of the true temperature. However, we find that the best-fit values are significantly biased high with respect to the input values for low counts, particularly for high temperatures $kT \geq 3$ keV. This study shows that we need to apply a significant correction to at least half of our sample. In our spectral analysis we will invert equation 1 to correct the best-fit temperature values obtained as a direct output of the spectral fits.

In Figure 8 we show the results for the iron abundance. We notice that here there is no clear dependence on the temperature, while the abundance measurements is seriously compromised below 300 net counts. Therefore, we simply decide to ignore the iron abundance measurements from spectra with less than

[2] We remind that the soft counts of sources SWXCS J000315-5255.2 and SWXCS J000324-5253.8 do not correspond to the actual counts in the spectra, since the source are overlapping and the soft-band photometry actually refer to the reconstructed circular regions. As a consequence, they have less than 1500 total net counts in the 0.5-7 keV band despite the large soft band photometry reported in Table 2.

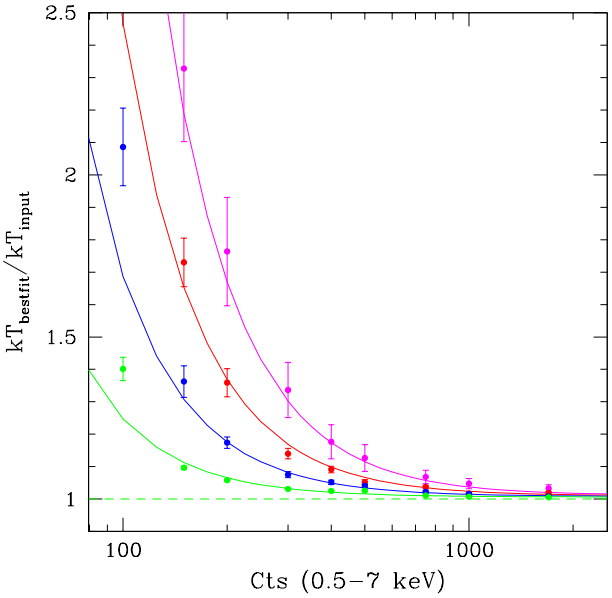

Fig. 7: Ratio of the best-fit over input temperature for our set of simulations, as a function of the total net counts in the 0.5-7 keV band. From top to bottom: magenta solid dots correspond to $kT = 7.5$ keV; red dots to 5 keV; blue dots to 3 keV; green dots to 1.5 keV. The corresponding lines show the best fit to the temperature bias function $R(T, cts)$ (see equation 1).

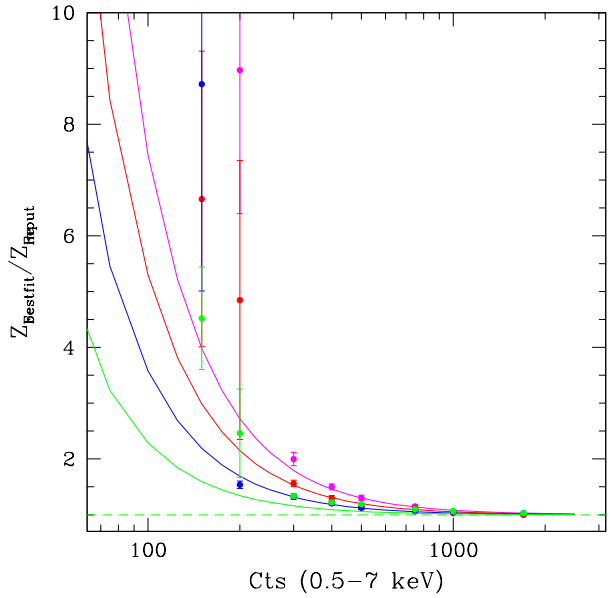

Fig. 8: Ratio of the best-fit over input abundance for our set of simulations, as a function of the total net counts in the 0.5-7 keV band. Colors as in Figure 7. The solid lines show the best fit to the abundance bias function $R_{abund}(Cts)$.

300 net counts, and provide this approximation for the function $R(Z_{Fe-input}, Cts)$ only above 300 counts:

$$R(Z_{Fe-input}, Cts) = 1 + 4.3 \times \left(\frac{kT_{input}}{5}\right)^{1.0} \times \left(\frac{Cts}{100}\right)^{-1.9}. \quad (2)$$

To summarize, our simulations show that it is possible to extend the X-ray spectral analysis down to very low counts, provided that one accounts for the fitting bias. The set of simulations investigated in this work provides a good approximation to the bias affecting the best-fit spectral parameters for our sample. Ideally, massive spectral simulations should be run for each source, in order to accurately reproduce the actual S/N regime of the spectrum. However, this extremely time-consuming approach is mandatory if one wants to use large X-ray cluster samples in the faint regime to investigate the statistical properties of the ICM and constrain the cosmological models. As a final comment, one may argue that adopting the χ^2 statistics may help in reducing the bias on the temperature found for the Cash statistics. However, we find that the χ^2 statistics performs much worse as far as the iron abundance is concerned, confirming once again that the Cash statistics should be preferred if the identification of the iron emission lines is a key step of the method. A detailed comparison of χ^2 vs Cash statistics under different circumstances need to be addressed by a dedicated extensive study which goes far beyond the scope of this work.

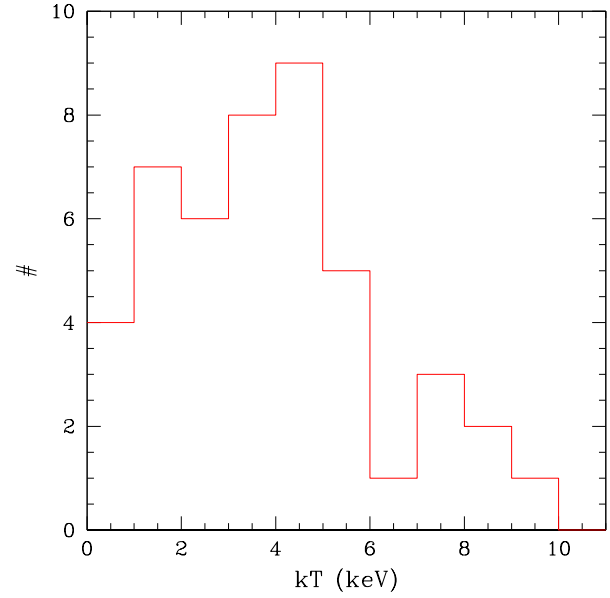

Fig. 9: ICM temperature distribution from X-ray spectral analysis, after accounting for fitting bias, for the 46 sources with redshift.

6. X-ray spectral analysis

6.1. Temperature and Fe abundance

We run the X-ray spectral analysis for all the 46 sources with available redshift, keeping fixed the redshift value. We use Cash statistics after re-binning the spectra to a minimal value of one count per bin (see Willis et al. 2005). We obtain a measure of the temperature for all our sources, irrespective of the S/N. In fact, once the redshift is fixed, the steepness of the spectrum in the hard band (2-7 keV) provide a simple means of constraining the global temperature even with a low S/N. Clearly, the pres-

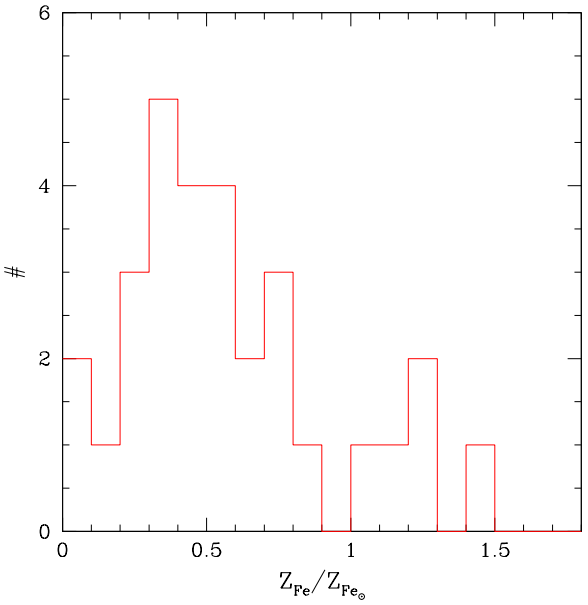

Fig. 10: Distribution of the bias-corrected values for the ICM iron abundance from X-ray spectral analysis for the 30 sources with redshift and more than 300 total net counts in the spectrum.

ence of a multi-temperature ICM, in particular the presence of cold gas in a cool-core, would be practically unnoticed, and its presence may, in some cases, bias the value of the global temperature. This effect cannot be treated on each single source with XRT data, due to the limited angular resolution. Another possible source of uncertainty is the presence of non-thermal emission due to a central AGN. Due to the limited angular resolution, it is not possible to identify and remove a possible contribution from a central AGN. Statistically, the contribution to the X-ray emission from AGN in clusters amounts to few percent (as found, for example, from the X-ray analysis of optically selected clusters, see Bignamini et al. (2008), therefore we neglect this contribution in our analysis. However, in at least two sources, SWXCS J094816-1316.7 and SWXCS J133055+4200.3, the best fit with a single `mekal` model, fails to reproduce the emission above 2 keV. For these two sources only we add an absorbed power law component with a fixed spectral slope $\Gamma = 1.8$, in order to properly account also for the hard-band emission.

Then, we apply the correction factor we derived in section 5. We find that, on average, the corrected temperatures are about 10% lower than the best-fit values. Global temperatures are measured with a typical 1σ error of 15% for the lower errorbar and 20% for the upper errorbar. In Figure 9 we show the distribution of the biased-corrected temperatures for the 46 sources with redshift. Half of the sources have temperatures between 3 and 6 keV, and the highest temperature is about 10 keV. Only 17 sources are classified as groups or low-mass clusters, simply on the basis of their ICM temperature below 3 keV. This shows that our sample ranges from groups to hot, massive clusters. Direct best-fit temperatures and their values corrected for fitting bias, with $1\ \sigma$ error bars, are listed in the third and fourth columns of Table 2.

The presence of the *K–shell* iron emission line complex at 6.7-6.9 keV rest-frame, allows us to measure an iron abundance larger than zero at $2\ \sigma$ for about 17 sources out of 30 with more than 300 net counts. The typical $1\ \sigma$ uncertainty on the iron abundance for the sources with iron line detection, is about 35% for the lower error bar and 50% for the upper error bar. For the sources with global temperatures below 3 keV, the iron abundance is measured also thanks to the increasing contribution of the *L–shell* emission lines in the energy range 1 – 2 keV. We remark that the iron abundance is slightly biased towards high values for clusters whose redshift is provided by the X-ray spectral analysis (see Yu et al. 2011). The contribution of elements other than iron is negligible, therefore we consider the best fit values as a measure of the iron abundance and not of the global metallicity, despite the abundance parameter in the `mekal` model refers to the global metallicity. As a robustness check, we repeat the fits with `vmekal` setting all the other elements to zero, and we find no changes with respect to the `mekal` values. The distribution of iron abundance values is shown in Figure 10, and it is consistent with distribution broadly peaked around $Z_{Fe} = 0.5 Z_{Fe\odot}$ in units of Asplund et al. (2005). Best-fit iron abundances and the corrected values for sources with more than 300 net counts are listed in the fifth and sixth columns of Table 2.

Despite the large statistical errors, we explore the correlation between measured iron abundance with temperature and redshift. In Figure 11 we show the iron abundance versus the measured temperature for sources with more than 300 net counts. The data are in broad agreement with a constant $Z_{Fe} \sim 0.5 Z_{Fe\odot}$ at temperature higher than 5 keV, a higher iron abundance between 3 and 5 keV, and lower values of Z_{Fe} towards the group scales, as previously noticed by Baumgartner et al. (2005) for local clusters and by Balestra et al. (2007) at higher redshift. However, the large uncertainties hampers us from drawing any conclusion. When comparing the iron abundance versus redshift (Figure 12) with Balestra et al. (2007) we find that the average Z_{Fe} tends to be lower at redshift $z \leq 0.2$ (see also Maughan et al. (2008)). Once again, the statistical uncertainties associated to our measurements of Z_{Fe} prevent us from performing a meaningful statistical analysis. We conclude that to investigate the behavior of the iron abundance with temperature and cosmic epoch, we would need a significantly higher S/N.

6.2. Cluster luminosities

Our spectral fits with a single `mekal` model provide also a measurement of the observed flux and the rest-frame luminosity, whose values are only marginally affected by the $\sim$ 10% correction on the best-fit temperatures. These soft-band flux values are more accurate than those obtained in Paper I, which were estimated on the basis of a simple energy conversion factor after accounting for the Galactic absorption in the corresponding field. In Figure 13 we plot our soft-band fluxes from X-ray spectral fits versus those obtained with the conversion factor, finding a very good agreement. We note that we do not use the values shown in Table 2 of Paper I, which refer to the flux within $2 \times R_{ext}$, but we consistently use those corresponding to R_{ext}, typically 5% lower. In addition, we do not include the two clusters SWXCS J000315-5255.2 and SWXCS J000324-5253.8, since for both objects, the spectral fit has been performed in the non-overlapping regions, while in Paper I the flux within R_{ext} has been reconstructed by extrapolating the surface brightness profile in the overlapping sectors. We find that the difference between the fluxes estimated with ECFs and the more accurate values obtained from the spectral fits, amounts on average to 1-2%, confirming that the use of ECFs is a very reliable method to estimate the fluxes in the soft band for both groups and clusters.

Finally, we computed the X-ray soft band and bolometric rest-frame luminosities within R_{ext} integrating over the entire

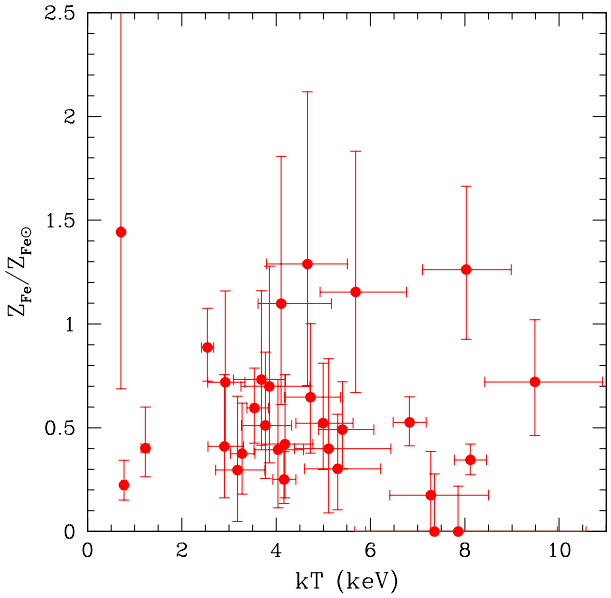

Fig. 11: Plot of iron abundance and global temperature for the 30 sources with X-ray spectral analysis and more than 300 net counts in the spectrum.

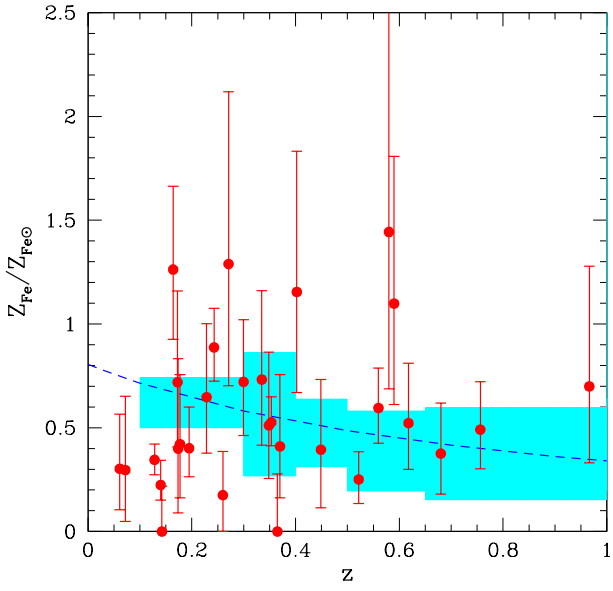

Fig. 12: Plot of iron abundance and redshift for the 30 sources with X-ray spectral analysis and more than 300 net counts in the spectrum. The shaded area correspond to the iron abundance average values measured with *Chandra* in Balestra et al. (2007), and the dashed line corresponds to their best fit. Values from Balestra et al. (2007) are re-scaled to the solar abundance of Asplund et al. (2005).

X-ray band, adopting a ΛCDM cosmology with $\Omega_m = 0.28$, $\Omega_\Lambda = 0.72$ and $H_0 = 69.7$ km s^{-1} Mpc^{-1}. We also compute the luminosity within R_{500} (defined as the radius within which the average density contrast is 500) extrapolating the surface brightness model at $R > R_{ext}$. The radius R_{500} is estimated from the corrected temperature using the empirical relation found by Vikhlinin et al. (2006):

$$R_{500} = 1.14 \times h^{-1} \times (\Omega_m (1+z)^3 + \Omega_\Lambda)^{0.5} \times (kT/10 \text{ keV})^{0.53} \text{ Mpc}\,, \quad (3)$$

where $h \equiv H_0/(100\,\mathrm{km\,s^{-1}\,Mpc^{-1}})$. In general the estimated R_{500} is larger than the extraction radius R_{ext} by a factor ranging from 1 to 4, with an average of ~ 2.9[3]. The luminosity outside the extraction region is computed extrapolating the fit to the surface brightness distribution as in Paper I. Errors on the luminosities are taken from the Poissonian error on the net detected counts, plus the uncertainty on the factor accounting for the missing flux outside R_{ext}. Soft-band and bolometric luminosities are listed in the last two columns of Table 2.

6.3. Luminosity-Temperature relation

In Figure 14, we plot the relation of bolometric luminosity versus the corrected temperature for the 46 sources with X-ray spectral analysis. We perform a simple linear regression in the log-log space, which is dominated by the error on the temperature. Our fitting function is

$$log(L_{500}) = C_0 + \alpha \times log(kT/5 \text{ keV})\,. \quad (4)$$

Despite the data present a significant intrinsic scatter, we consider the entire range of temperature and luminosities to search for a best fit. We find $C_0 = 44.6 \pm 0.03$ and $\alpha = 2.8 \pm 0.12$. Our best-fit relation is compared to the $L_X - T_X$ relation obtained by Branchesi et al. (2007b) and by Maughan et al. (2012). We adopt the $L_X - T_X$ relation obtained for all the clusters, including the core regions, in Maughan et al. (2012), and correct for the $E(z)$ factor (which is not used in our analysis) by assuming as a representative redshift for our sample $\langle z \rangle = 0.25$. We also use the $L_X - T_X$ relation obtained for the combined sample in Branchesi et al. (2007b) and computed for the same average redshift $\langle z \rangle = 0.25$. The slope of our best fit $L_X - T_X$ relation is somewhat shallower but still in agreement within 1 σ with the value $\alpha = 3.05 \pm 0.23$ found by Branchesi et al. (2007b), while is significantly shallower with respect to $\alpha = 3.63 \pm 0.27$ found by Maughan et al. (2012). The normalization of the best-fit relation is in good agreement with both works. We note, however, that our sample includes many more low-mass clusters and groups, while the sample in the two quoted papers are dominated by clusters with $L_X > 10^{44}$ erg s^{-1}. If we fit only the bright part of our sample at luminosities higher than 10^{44} erg s^{-1}, we find a 15% lower normalization and a steeper slope $\alpha = 3.4 \pm 0.4$. We also remark that selection effects are difficult to model for a sample drawn directly from the *Chandra* archive, without a well defined selection function. A meaningful comparison of the scaling properties of the X-ray observables between the SWXCS and previous studies would require a larger statistics, which we expect to reach with the spectral analysis of the final SWXCS sample, taking advantage of its accurately modeled selection function.

[3] We remark that the values of R_{ext} listed in Table 2 of Paper I are in pixels and not in arcsec as erroneously written in the caption of the Table. Here we report the correct values in arcmin, obtained assuming the conversion factor of 2.36 arcsec per pixel.

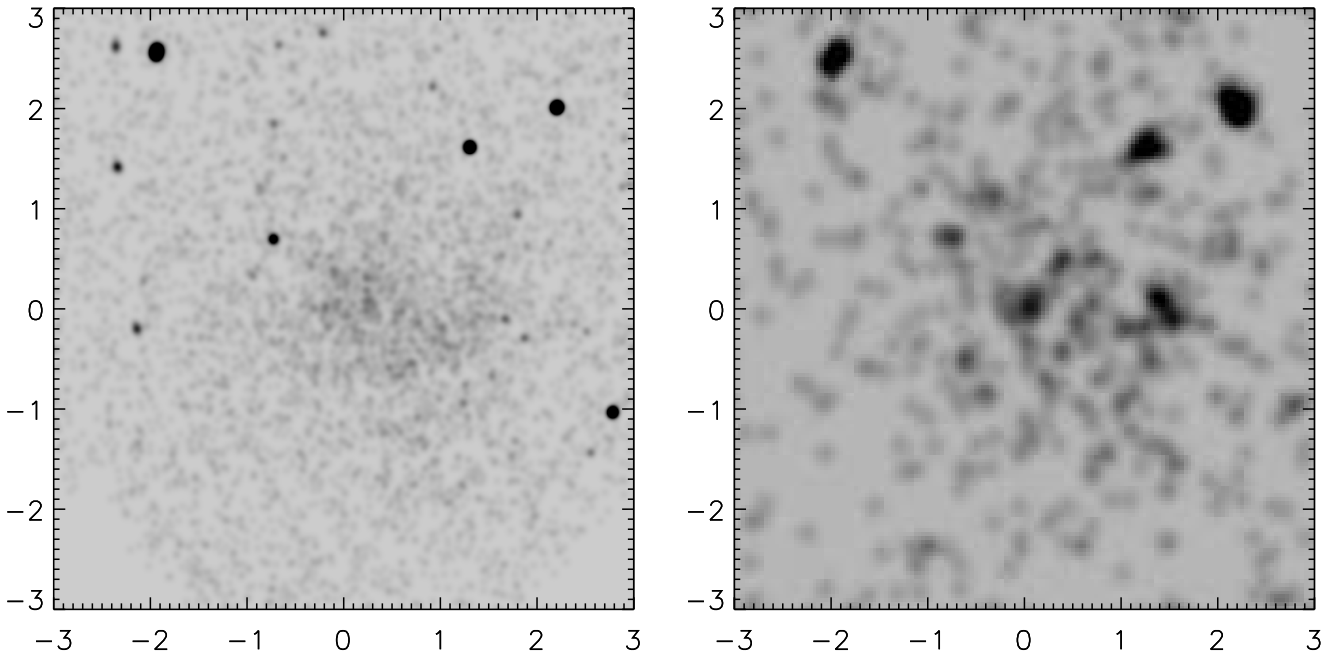

Fig. 15: ACIS-S Chandra 50 ks image (left panel) and XRT 34 ks image (right panel) of SWXCS J123630+2859.1 at $z_{spec} = 0.23$. Both images are in the soft [0.5-2] keV band and Gaussian smoothed with a FWHM of 10 and 5 arcsec respectively. The scale of the image is 7 arcmin. The difference of the image quality is striking due to the two order of magnitude difference in angular resolution, however the quality of the spectral analysis based on these data is comparable owing to the low XRT background and good hard energy response (see text).

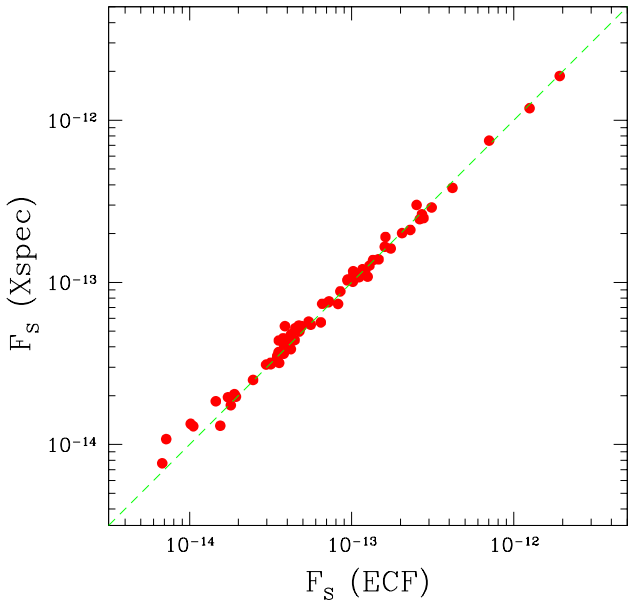

Fig. 13: Soft-band fluxes obtained directly from the X-ray spectral analysis, compared to the soft band fluxes measured in Paper I assuming a simple energy conversion factor. Dashed line shows the $F_S(Xspec) = F_S(ECF)$ relation.

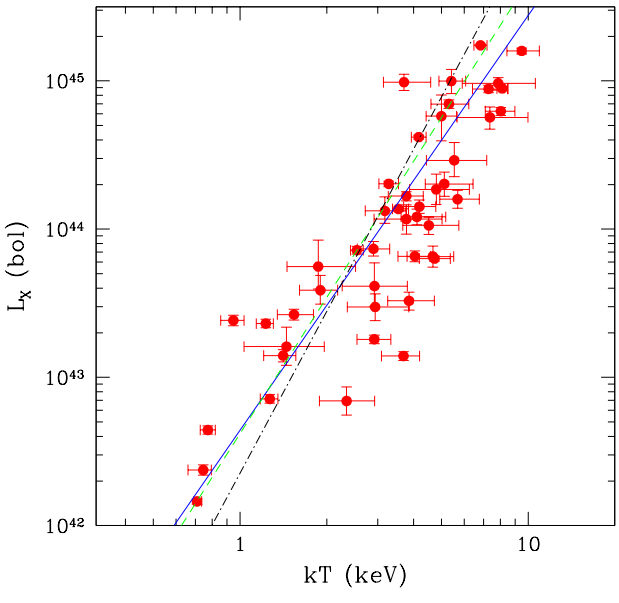

Fig. 14: $L_X - T_X$ relation for the 46 sources with spectral analysis. The solid blue line is the best fit of the $L_X - T_X$ for our sample. The dashed green line is the best fit for the combined cluster sample analyzed by Branchesi et al. (2007b) computed for $\langle z \rangle = 0.25$, while the black, dot-dashed line is for the "all cluster" sample presented in Maughan et al. (2012) and computed for $\langle z \rangle = 0.25$. Luminosities are consistently computed at the estimated radius R_{500}. Error bars correspond to 1 σ error both in temperature and luminosity.

7. A Chandra observation of an SWXCS cluster

We take advantage of a set of *Chandra* follow-up observations of Swift GRB to search for *Chandra* images of our extended sources. Unfortunately, the use of ACIS-S, which has a significantly smaller FOV with respect to XRT, further reduces the probability of having *Chandra* data for our sources. We find two Swift GRBs observed with *Chandra* whose fields contain a SWXCS cluster: GRB050509 (SWXCS J123620+2859.1) and GRB052120 (SWXCS J215507+1647.3). Only the first one, however, covers our source with the ACIS S3 chip, while in the second case our source is at very large off-axis angle ($\sim$ 10 arcmin) and it lies in an ancillary CCD, therefore its imaging and spectral quality are not sufficient for a robust analysis. In the following we will discuss only the *Chandra* observation of SWXCS J123620+2859.1.

SWXCS J123620+2859.1 has a 50 ks observation with *Chandra* ACIS-S (ObsId 5588). We collect about 1700 net photons in the 0.5-7 keV band, corresponding to a total flux of 1.3×10^{-13} erg s^{-1} cm^{-2} within the same extraction radius of 90 arcsec, consistent with the flux measured with the XRT data. Our spectral fit with free redshift returns a values $z_X = 0.20 \pm 0.02$, in very good agreement with the spectroscopic redshift $z_{spec} = 0.23 \pm 0.01$ (see Table 1). We obtain $kT = (3.6 \pm 0.6)$ keV and $Z_{Fe} = 0.6^{+0.4}_{-0.3} Z_\odot$, in agreement within 1 σ with the value found with the XRT analysis, based only on $\sim$ 200 net counts in the 0.5-7 keV. From XRT we obtain $kT = 4.6^{+1.5}_{-1.1}$ keV directly from the best-fit, and $kT = 3.8^{+1.2}_{-0.9}$ keV after the correction for the fitting bias. As for the iron abundance, we only obtain a loose upper limit of $Z_{Fe} < 0.40 Z_\odot$ at 1 σ c. l. Therefore, using about eight times fewer photons than those collected by *Chandra* in the same band, we obtain a consistent temperature value with error bars larger by a factor of two. This simple comparison practically shows the good performance of a small instrument like XRT for the study of faint extended sources, despite the poor image quality when compared to the Chandra soft-band image (see Figure 15). Both the low background and the relatively high response function in the hard band (see Figure 1 in Paper I) contribute to provide a reliable estimate of the temperature for this cluster despite the low S/N. We argue that an instrument built as a larger version of the XRT, with a comparably low background and with a better angular resolution, would be extremely efficient in finding and characterizing groups and clusters of galaxies down to very low fluxes.

8. Conclusions

We present detailed spectral analysis for the X-ray groups and clusters of galaxies in the SWXCS catalog (Tundo et al. 2012). We retrieve the optical spectroscopic or photometric redshift for 35 sources out of 72, thanks to the cross-correlation with the NASA/IPAC Extragalactic Database and a dedicated TNG follow-up program. A blind search of the iron K_α emission line complex in the X-ray spectra of our sources with optical redshift, allows us to set the criteria for a reliable measurement of the redshift from the X-ray spectra alone. Therefore, we are able to extend our X-ray redshift measurement to the entire sample, finding another 11 reliable redshifts, for a total of 46 out of 72 sources in total. The redshift distribution is peaked around $z \sim 0.2$, with a tail extending up to $z \sim 0.9$. We find that 12 sources (25% of those with redshift) have redshift larger than 0.4.

Despite the relatively low S/N of our sample, we are able to measure the temperature for all our sources with redshift, with typical 1 σ errorbars of 15-20%. We explore the robustness of our X-ray spectral analysis with extensive spectral simulations, deriving correction factors for temperature and abundance depending on the actual temperature of the source and on the total (0.5-7 keV) net counts in the source spectrum. After accounting for this fitting bias, we find that the corrected temperatures are on average $\sim$ 10% lower than the values obtained directly from *Xspec*. We also find that abundance measurements are not reliable when the total net counts in the spectrum is lower than 300. Despite this, we are also able to estimate the iron abundance in several cases, although the large statistical uncertainties do not allow us to draw conclusions on the correlation of iron abundance with temperature or redshift. We find that about 60% of our sources have global temperatures in the range of massive clusters ($kT > 3$ keV), with only 17 sources with temperatures typical of groups ($kT < 3$ keV). We also measure the rest-frame, soft and bolometric luminosities up to R_{500}, where we estimated R_{500} from the temperature itself, and extrapolated the surface brightness profile beyond the extraction radius up to R_{500} to evaluate the missing fraction of the flux. We are then able to compute the $L_X - T_X$ relation, finding a slightly shallower slope with respect to previous studies, but overall consistent normalization.

The major result of our study, is that for the first time we are able to characterize the majority of a flux-limited, X-ray cluster sample on the basis of the X-ray discovery data, without time-consuming follow-up observations, if not for a partial photometric campaign with the TNG. The characterization of the sample is not complete yet, since 26 sources still lack a redshift measurement. In the near future, we plan to complete the identification of the sources in the SWXCS catalog of Paper I, and eventually to extend our sample to lower fluxes and to a larger portion of the Swift-XRT archive, using a detection algorithm based on Voronoi tessellation and developed *ad hoc* for XRT data (see Liu et al. 2013, for a description of the algorithm). The final goal is to assemble a sizable sample with a good characterization, including mass proxies for the majority of the sample, and to use it for a robust determination of the cluster mass function at $M \lesssim M_*$ and $z \sim 0.5$.

To summarize, the SWXCS is a practical example of how to build an extremely simple and effective X-ray cluster sample, and it can be useful to design efficient surveys with future X-ray facilities. This result, despite the small size of the XRT telescope, has been achieved thanks to the well defined selection function associated to our detection strategy, and to some specific properties of the XRT, namely: the low background, the constant angular resolution across the field of view, and the good spectral response in the hard band (2-7 keV), which is crucial to measure temperature and iron emission lines. These properties are mandatory for assembling large sample of X-ray clusters for precision cosmology without time-prohibitive follow-up campaigns in other wavebands.

Acknowledgements. We thank Heinz Handernach for pointing out the overlap of some of our sources with Abell clusters, and for suggesting to register the acronym SWXCS to the IAU registry. We acknowledge support from ASI-INAF I/088/06/0 and ASI-INAF I/009/10/0. This work is also supported at OAB-INAF by ASI grant I/004/11/0. PT, AM, ET and TL received support from the "Exchange of Researchers" program for scientific and technological cooperation between Italy and the People's Republic of China for the years 2013-2015 (code CN13MO5). SB acknowledges partial financial support from the PRIN-MIUR 2009 grant "tracing the growth of cosmic structures" and from the PD51 INFN grant. This research has made use of the NASA/IPAC Extragalactic Database (NED) which is operated by the Jet Propulsion Laboratory, California Institute of Technology, under contract with the National Aeronautics and Space Administration. We also thank the anonymous Referee for comments and suggestions which significantly improved the paper.

References

Abazajian, K., Adelman-McCarthy, J. K., Agüeros, M. A., et al. 2005, AJ, 129, 1755
Abell, G. O., Corwin, Jr., H. G., & Olowin, R. P. 1989, ApJS, 70, 1
Adami, C., Mazure, A., Pierre, M., et al. 2011, A&A, 526, A18
Adelman-McCarthy, J. K., Agüeros, M. A., Allam, S. S., et al. 2008, ApJS, 175, 297
Adelman-McCarthy, J. K., Agüeros, M. A., Allam, S. S., et al. 2007, ApJS, 172, 634
Adelman-McCarthy, J. K., Agüeros, M. A., Allam, S. S., et al. 2006, ApJS, 162, 38
Allen, S. W., Evrard, A. E., & Mantz, A. B. 2011, ARA&A, 49, 409
Anderson, M. E., Bregman, J. N., Butler, S. C., & Mullis, C. R. 2009, ApJ, 698, 317
Arnaud, K., Smith, R., & Siemiginowska, A. 2011, Handbook of X-ray Astronomy, ed. R. Ellis, J. Huchra, S. Kahn, G. Rieke, & P. B. Stetson
Arnaud, K. A. 1996, in Astronomical Society of the Pacific Conference Series, Vol. 101, Astronomical Data Analysis Software and Systems V, ed. G. H. Jacoby & J. Barnes, 17–+
Asplund, M., Grevesse, N., & Sauval, A. J. 2005, in Astronomical Society of the Pacific Conference Series, Vol. 336, Cosmic Abundances as Records of Stellar Evolution and Nucleosynthesis, ed. T. G. Barnes III & F. N. Bash, 25–+
Balestra, I., Tozzi, P., Ettori, S., et al. 2007, A&A, 462, 429
Barthelmy, S. D., Barbier, L. M., Cummings, J. R., et al. 2005, Space Sci. Rev., 120, 143
Baumgartner, W. H., Loewenstein, M., Horner, D. J., & Mushotzky, R. F. 2005, ApJ, 620, 680
Bertin, E. & Arnouts, S. 1996, A&AS, 117, 393
Bevington, P. R. & Robinson, D. K. 2003, Data reduction and error analysis for the physical sciences
Bignamini, A., Tozzi, P., Borgani, S., Ettori, S., & Rosati, P. 2008, A&A, 489, 967
Böhringer, H. & Werner, N. 2010, A&A Rev., 18, 127
Bolzonella, M., Miralles, J.-M., & Pelló, R. 2000, A&A, 363, 476
Borgani, S. 2008, in Lecture Notes in Physics, Berlin Springer Verlag, Vol. 740, A Pan-Chromatic View of Clusters of Galaxies and the Large-Scale Structure, ed. M. Plionis, O. López-Cruz, & D. Hughes, 287
Borm, K., Reiprich, T. H., Mohammed, I., & Lovisari, L. 2014, ArXiv:1404.5312
Branchesi, M., Gioia, I. M., Fanti, C., & Fanti, R. 2007a, A&A, 472, 727
Branchesi, M., Gioia, I. M., Fanti, C., & Fanti, R. 2007b, A&A, 472, 739
Bruzual, G. & Charlot, S. 2003, MNRAS, 344, 1000
Burenin, R. A., Vikhlinin, A., Hornstrup, A., et al. 2007, ApJS, 172, 561
Burrows, D. N., Hill, J. E., Nousek, J. A., et al. 2005, Space Sci. Rev., 120, 165
Cash, W. 1979, ApJ, 228, 939
Citterio, O., Conconi, P., Ghigo, M., et al. 1994, in Society of Photo-Optical Instrumentation Engineers (SPIE) Conference Series, Vol. 2279, Society of Photo-Optical Instrumentation Engineers (SPIE) Conference Series, ed. R. B. Hoover & A. B. Walker, 480–492
Colless, M., Dalton, G., Maddox, S., et al. 2003, VizieR Online Data Catalog, 7226, 0
di Nella, H., Couch, W. J., Paturel, G., & Parker, Q. A. 1996, MNRAS, 283, 367
Estrada, J., Annis, J., Diehl, H. T., et al. 2007, ApJ, 660, 1176
Ettori, S., Tozzi, P., Borgani, S., & Rosati, P. 2004, A&A, 417, 13
Evans, P. A., Beardmore, A. P., Page, K. L., et al. 2009, MNRAS, 397, 1177
Fassbender, R., Böhringer, H., Nastasi, A., et al. 2011, New Journal of Physics, 13, 125014
Gal, R. R., de Carvalho, R. R., Lopes, P. A. A., et al. 2003, AJ, 125, 2064
Gehrels, N., Chincarini, G., Giommi, P., et al. 2004, ApJ, 611, 1005
Hao, J., McKay, T. A., Koester, B. P., et al. 2010, ApJS, 191, 254
Hinshaw, G., Larson, D., Komatsu, E., et al. 2013, ApJS, 208, 19
Huchra, J. P., Macri, L. M., Masters, K. L., et al. 2012, ApJS, 199, 26
Kaastra, J. 1992, An X-Ray Spectral Code for Optically Thin Plasmas (Internal SRONLeiden Report, updated version 2.0)
Kalberla, P. M. W., Burton, W. B., Hartmann, D., et al. 2005, A&A, 440, 775
Koester, B. P., McKay, T. A., Annis, J., et al. 2007, ApJ, 660, 239
Kravtsov, A. V. & Borgani, S. 2012, ARA&A, 50, 353
Kravtsov, A. V., Vikhlinin, A., & Nagai, D. 2006, ApJ, 650, 128
Lauberts, A. 1982, ESO/Uppsala survey of the ESO(B) atlas
Liedahl, D. A., Osterheld, A. L., & Goldstein, W. H. 1995, ApJ, 438, L115
Liu, T., Tozzi, P., Tundo, E., et al. 2013, A&A, 549, A143
Lloyd-Davies, E. J., Romer, A. K., Mehrtens, N., et al. 2011, MNRAS, 418, 14
Lopes, P. A. A., de Carvalho, R. R., Gal, R. R., et al. 2004, AJ, 128, 1017
Lumsden, S. L., Nichol, R. C., Collins, C. A., & Guzzo, L. 1992, MNRAS, 258, 1
Mantz, A., Allen, S. W., Rapetti, D., & Ebeling, H. 2010, MNRAS, 406, 1759
Markevitch, M. & Vikhlinin, A. 2007, Phys. Rep., 443, 1
Maughan, B. J., Giles, P. A., Randall, S. W., Jones, C., & Forman, W. R. 2012, MNRAS, 421, 1583
Maughan, B. J., Jones, C., Forman, W., & Van Speybroeck, L. 2008, ApJS, 174, 117
McNamara, B. R. & Nulsen, P. E. J. 2007, ARA&A, 45, 117
Merloni, A., Predehl, P., Becker, W., et al. 2012, ArXiv:1209.3114
Miller, C. J., Nichol, R. C., Reichart, D., et al. 2005, AJ, 130, 968
Moretti, A., Gastaldello, F., Ettori, S., & Molendi, S. 2011, A&A, 528, A102
Moretti, A., Perri, M., Capalbi, M., et al. 2007, in Society of Photo-Optical Instrumentation Engineers (SPIE) Conference Series, Vol. 6688, Society of Photo-Optical Instrumentation Engineers (SPIE) Conference Series
Moretti, A., Vattakunnel, S., Tozzi, P., et al. 2012, A&A, 548, A87
Murray, S. S., Giacconi, R., Ptak, A., et al. 2010, in Society of Photo-Optical Instrumentation Engineers (SPIE) Conference Series, Vol. 7732, Society of Photo-Optical Instrumentation Engineers (SPIE) Conference Series
Nousek, J. A. & Shue, D. R. 1989, ApJ, 342, 1207
Owen, F. N., Ledlow, M. J., & Keel, W. C. 1995, AJ, 109, 14
Planck Collaboration, Ade, P. A. R., Aghanim, N., et al. 2013a, ArXiv:1303.5089
Planck Collaboration, Ade, P. A. R., Aghanim, N., et al. 2013b, ArXiv:1303.5076
Planck Collaboration, Ade, P. A. R., Aghanim, N., et al. 2013c, ArXiv:1303.5080
Predehl, P., Böhringer, H., Brunner, H., et al. 2010, in American Institute of Physics Conference Series, Vol. 1248, American Institute of Physics Conference Series, ed. A. Comastri, L. Angelini, & M. Cappi, 543–548
Reichardt, C. L., Stalder, B., Bleem, L. E., et al. 2013, ApJ, 763, 127
Rosati, P., Borgani, S., Gilli, R., et al. 2011, Memorie della Societa Astronomica Italiana Supplementi, 17, 8
Rosati, P., Borgani, S., & Norman, C. 2002, ARA&A, 40, 539
Rosati, P., della Ceca, R., Norman, C., & Giacconi, R. 1998, ApJ, 492, L21+
Santos, J. S., Rosati, P., Tozzi, P., et al. 2008, A&A, 483, 35
Santos, J. S., Tozzi, P., Rosati, P., & Böhringer, H. 2010, A&A, 521, A64
Schuecker, P. 2005, in Reviews in Modern Astronomy, Vol. 18, Reviews in Modern Astronomy, ed. S. Röser, 76–105
Schwope, A., Hasinger, G., Lehmann, I., et al. 2000, Astronomische Nachrichten, 321, 1
Sehgal, N., Trac, H., Acquaviva, V., et al. 2011, ApJ, 732, 44
Shectman, S. A., Landy, S. D., Oemler, A., et al. 1996, ApJ, 470, 172
Struble, M. F. & Rood, H. J. 1999, ApJS, 125, 35
Szabo, T., Pierpaoli, E., Dong, F., Pipino, A., & Gunn, J. 2011, ApJ, 736, 21
Tundo, E., Moretti, A., Tozzi, P., et al. 2012, A&A, 547, A57
Šuhada, R., Song, J., Böhringer, H., et al. 2012, A&A, 537, A39
Vikhlinin, A., Kravtsov, A., Forman, W., et al. 2006, ApJ, 640, 691
Vikhlinin, A., Kravtsov, A. V., Burenin, R. A., et al. 2009, ApJ, 692, 1060
Voit, G. M. 2005, Rev. Mod. Phys., 77, 207
von der Linden, A., Best, P. N., Kauffmann, G., & White, S. D. M. 2007, MNRAS, 379, 867
Wen, Z. L., Han, J. L., & Liu, F. S. 2009, ApJS, 183, 197
Wen, Z. L., Han, J. L., & Liu, F. S. 2010, ApJS, 187, 272
Wen, Z. L., Han, J. L., & Liu, F. S. 2012, ApJS, 199, 34
Willis, J. P., Pacaud, F., Valtchanov, I., et al. 2005, MNRAS, 363, 675
Wilms, J., Allen, A., & McCray, R. 2000, ApJ, 542, 914
Yu, H., Tozzi, P., Borgani, S., Rosati, P., & Zhu, Z.-H. 2011, A&A, 529, A65
Zwicky, F., Herzog, E., & Wild, P. 1963, Catalogue of galaxies and of clusters of galaxies, Vol. 2

Table 1. Cluster sample. (i) Cluster name; (ii) optical redshift from cross-correlation with the NED; (iii) photometric redshift from follow-up with TNG (one case, marked with *, obtained with VLT archival data); (iv) X-ray redshift; (v) reference for optical redshift; (vi) name of the optical counterpart (cluster); (vii) name of the optical counterpart (galaxy); (viii) name of the X-ray source as in Paper I. The format of the name of the sources is SWXCS JHHMMSS+DDMM.m. This new designation supersedes that used in Paper I, and it has been officially accepted by the IAU register of acronym. References for the redshifts from the Literature: [1] Shectman et al. (1996); [2]Colless et al. (2003); [3]Adelman-McCarthy et al. (2006); [4] Wen et al. (2010); [5] Adelman-McCarthy et al. (2008); [6] Koester et al. (2007); [7] Abazajian et al. (2005); [8] Hao et al. (2010); [9] von der Linden et al. (2007); [10] Huchra et al. (2012); [11] Gal et al. (2003); [12]Adelman-McCarthy et al. (2007); [13]Estrada et al. (2007); [14]Owen et al. (1995); [15]Struble & Rood (1999); [16]Schwope et al. (2000); [17]di Nella et al. (1996); [18] redshift obtained from Literature by the NED Team prior to November 1992; [19]Szabo et al. (2011). The source marked with * has two other cluster counterparts at distances larger than 1 arcmin from the X-ray centroid: ZwCl 1234.0+2916 and WHL J123620.6+285756. These counterparts are not considered here.

name	z_{opt} (NED)	z_{opt} (TNG)	z_X	Ref. for z_{opt}	Optical counterpart (cluster)	Optical counterpart (galaxy)	Name as in Paper I
SWXCS J000345-5301.8							SWJ000345-530149
SWXCS J000315-5255.2			0.62 ± 0.1				SWJ000315-525510
SWXCS J000324-5253.8			0.76 ± 0.01				SWJ000324-525350
SWXCS J002437-5803.9			0.195 ± 0.012				SWJ002437-580353
SWXCS J003316+1939.4							SWJ003316+193922
SWXCS J005500-3852.4	0.164127 ± 0.000213 (s)			LCRS[1]	EDCC493	LCRS B005239.6-390844	SWJ005500-385226
SWXCS J011432-4828.4			0.97 ± 0.02				SWJ011432-482824
SWXCS J012210-1304.4							SWJ012210-130422
SWXCS J012302+3756.3							SWJ012302+375615
SWXCS J015753+1659.6							SWJ015753+165933
SWXCS J020744+0020.9							SWJ020744+002055
SWXCS J021705-5014.2			0.52 ± 0.01				SWJ021705-501409
SWXCS J021747-5003.4			0.206 ± 0.01				SWJ021747-500322
SWXCS J022344+3823.2							SWJ022344+382311
SWXCS J022546-1855.9							SWJ022546-185553
SWXCS J023224-7120.3							SWJ023224-712020
SWXCS J023302-7116.6							SWJ023302-711634
SWXCS J023924-2505.1	0.1737 ± 0.000213 (s)			2dFGRS[2]		2dFGRS S159Z145	SWJ023924-250504
SWXCS J024010-2511.3							SWJ024010-251121
SWXCS J035259-0043.7	0.334925 ± 0.000293 (s)		$0.31^{+0.02}_{-0.01}$	SDSS[3]		SDSSJ035259.38-004337.8	SWJ035259-004342
	0.325 ± 0.01 (p)		$0.31^{+0.02}_{-0.01}$	WHL[4]	WHLJ035259.4-004337		SWJ035259-004342
SWXCS J035310+2133.6							SWJ035310+213335
SWXCS J044144-1115.6		0.26 ± 0.02	$0.193^{+0.01}_{-0.015}$				SWJ044144-111536
SWXCS J062155-6228.6			$0.35^{+0.02}_{-0.01}$				SWJ062155-622834
SWXCS J082113+3200.1		0.68 ± 0.06					SWJ082113+320004
SWXCS J083340+3311.0							SWJ083340+331102
SWXCS J084749+1331.7	0.363 ± 0.01 (p)	0.35 ± 0.01	0.349 ± 0.005	WHL[4]	WHLJ084749.3+133140		SWJ084749+133141
	0.348628 ± 0.000147 (s)	0.35 ± 0.01	0.349 ± 0.005	SDSS[5]		SDSSJ084749.32+133140.4	SWJ084749+133141
SWXCS J085524+1102.0		0.37 ± 0.01					SWJ085524+110201
SWXCS J090946+4157.2	0.14855 ± 0.01 (p)		0.171 ± 0.02	WHL[6]	WHL J090945.9+415721		SWJ090946+415713
	0.140048 ± 0.000175 (s)		0.171 ± 0.02	SDSS [7]		B3 0906+421	SWJ090946+415713
SWXCS J092619-0905.8							SWJ092619-090546
SWXCS J092729+3010.8	0.365 ± 0.01 (p)			WHL[4]	WHLJ092730.0+301045		SWJ092729+301048
	0.293 ± 0.01 (p)			SDSS[8]		SDSS J092730.01+301045.4	SWJ092729+301048
SWXCS J092650+3013.8		0.58 ± 0.07	0.418 ± 0.008				SWJ092650+301345
SWXCS J092719+3013.7	0.29975 ± 0.01 (p)			WHL[6]	WHLJ092719.8+301355		SWJ092719+301342
SWXCS J093045+1659.5	0.177278 ± 0.000165 (s)			2MASX[5]		2MASX J09304539+1659294	SWJ093045+165931
SWXCS J093749+1535.7	0.271 ± 0.01 (p)		$0.322^{+0.020}_{-0.045}$	GMBCG[8]	GMBCG J144.45579+15.59434		SWJ093749+153540
	0.294 ± 0.01 (p)		$0.322^{+0.020}_{-0.045}$	AMF[19]	AMFJ144.4580+15.5998		SWJ093749+153540
	0.271 ± 0.01 (p)		$0.322^{+0.020}_{-0.045}$	SDSS [8]		SDSS J093749.38+153539.6	SWJ093749+153540
SWXCS J094816-1316.7			0.13 ± 0.02				SWJ094816-131644
SWXCS J101341+4306.9	0.44886 ± 0.000217 (s)			SDSS[7]		SDSS J101341.77+430656.6	SWJ101341+430655

Table 1. continued.

name	z_{opt} (NED)	z_{opt} (TNG)	z_X	Ref for z_{opt}	Optical counterpart (cluster)	Optical counterpart (galaxy)	name as in Paper I
SWXCS J105946+5348.2	0.072 ± 0.01 (p)		0.12 ± 0.02	SDSS[9]	SDSS-C4-DR3 3205		SWJ105946+534809
	0.071199 ± 0.000097 (s)		0.12 ± 0.02	2MASS[10]		MCG +09-18-064	SWJ105946+534809
SWXCS J115811+4529.1	0.4024 ± 0.01 (p)			WHL[4]	WHLJ115814.4+452930		SWJ115811+452906
	0.4051 ± 0.01 (p)			AMF[19]	AMFJ179.5554+45.4806		SWJ115811+452906
SWXCS J123620+2859.1*	0.243 ± 0.01 (p)			GMBCG[8]	GMBCG J189.08767+28.99149		SWJ123620+285905
	0.2305 ± 0.01 (p)			AMF[19]	AMFJ189.0796 +28.9838		SWJ123620+285905
	0.228573 ± 0.00017 (s)			SDSS[5]		2MASXJ12362010+2859080	SWJ123620+285905
SWXCS J124312+1704.9	0.1424 ± 0.01 (p)			NSCS[11]	NSCS J124308+170537		SWJ124312+170451
SWXCS J131300+0803.0	0.5598 ± 0.01 (p)			WHL[5]	WHLJ131300.1+080303		SWJ131300+080259
SWXCS J131522+1641.8							SWJ131522+164145
SWXCS J133055+4200.3	0.061154 ± 0.000197 (s)		$0.06^{+0.01}_{-0.02}$	SDSS[12]		2MASXJ13305564+4200176	SWJ133055+420017
SWXCS J133051+4206.8							SWJ133051+420647
SWXCS J140637+2743.8		0.59 ± 0.04					SWJ140637+274349
SWXCS J140639+2735.8	0.24305 ± 0.01 (s)			SDSS[6]	GMBCG J211.66393+27.59979		SWJ140639+273546
SWXCS J140728+2749.3	0.17255 ± 0.01 (p)			Abell[13]	Abell 1861		SWJ140728+274917
	0.17015 ± 0.01 (p)			SDSS[6]	WHLJ140726.6+274742		SWJ140728+274917
SWXCS J143646+2752.0	0.2648 0.01 (p)			AMF19	AMFJ219.2030 +27.8593		SWJ143646+275157
SWXCS J151324+3057.6	0.0717 ± 0.01 (p)			NED[18]	CGCG 165-032		SWJ151324+305738
SWXCS J155742+3530.4	0.169 ± 0.01 (p)		0.154 ± 0.004	SDSS[8]	GMBCG J239.42668+35.50827		SWJ155742+353023
	0.1549 ± 0.01 (p)		0.154 ± 0.004	SDSS	MaxBCG J239.42665+35.50827		SWJ155742+353023
	0.1459 ± 0.01 (p)		0.154 ± 0.004	SDSS[4]	WHL J155746.1+352954 239.44208		SWJ155742+353023
	0.16 ± 0.01 (s)		0.154 ± 0.004		Abell2141		SWJ155742+353023
	0.1579 ± 0.0004 (s)		0.154 ± 0.004	B2[14]		B2 1555+35B 239.42558	SWJ155742+353023
	0.158877 ± 0.000176 (s)		0.154 ± 0.004	SDSS[12]		2MASX J15574240+3530292	SWJ155742+353023
SWXCS J164956+3130.3							SWJ164956+313021
SWXCS J173721+4618.6		0.22 ± 0.02	0.29 ± 0.01				SWJ173721+461834
SWXCS J173932+2720.9							SWJ173932+272055
SWXCS J175640+3329.5			$0.195^{+0.02}_{-0.03}$				SWJ175640+332928
SWXCS J181053+5815.5							SWJ181053+581527
SWXCS J194004+7824.3							SWJ194004+782419
SWXCS J203723-4401.7							SWJ203723-440141
SWXCS J215507+1647.4							SWJ215507+164725
SWXCS J215354+1653.8		0.23 ± 0.02					SWJ215354+165348
SWXCS J222600-5712.8	0.13 ± 0.01 (p)		0.15 ± 0.01	Abell[15]	Abell3875		SWJ222600-571248
SWXCS J222443-0220.5							SWJ222443-022031
SWXCS J222516-0208.5							SWJ222516-020827
SWXCS J222437-0222.5							SWJ222437-022230
SWXCS J222917-1101.1		$0.20^{+0.01}_{-0.02}$	0.197 ± 0.02				SWJ222917-110106
SWXCS J222953+1943.9		0.24 ± 0.02	0.25 ± 0.01				SWJ222953+194354
SWXCS J224207+2333.9		0.71 ± 0.02					SWJ224207+233354
SWXCS J230754-6815.1			0.097 ± 0.02				SWJ230754-681505
SWXCS J230650-6804.0							SWJ230650-680401
SWXCS J232248+0548.2		$0.28^{+0.04}_{-0.07}$	0.226 ± 0.006				SWJ232248+054809
SWXCS J232345-3130.8		$0.85^{+0.07}_{-0.03}$ *		VLT			SWJ232345-313048
SWXCS J233518-6621.7			0.383 ± 0.009				SWJ233518-662139
SWXCS J233617-3136.5	0.0623 ± 0.01 (p)		0.068 ± 0.006	RBS[16]	AbellS1136		SWJ233617-313626
	0.06255 ± 0.000163 (s)		0.068 ± 0.006	ESO[17]	ESO 470- G 020		SWJ233617-313626

Table 2. Results of X-ray spectral analysis. (i) Source Name; (ii) radius of the circular region used for spectroscopic analysis; (iii) temperature directly obtained from the spectral analysis; (iv) temperature corrected for fitting bias; (v) iron abundance directly obtained from the spectral analysis; (vi) iron abundance corrected for the fitting bias; (vii) soft band flux measured within R_{ext}; (viii) soft band (0.5-2 keV) luminosity measured within R_{ext}; (ix) bolometric X-ray luminosity measured within R_{ext}; (x) soft net counts; (xi) estimated R_{500} in kpc; (xii) estimated R_{500} in arcmin; (xiii) estimated soft band (0.5-2 keV) luminosity within R_{500}; (xiv) estimated bolometric X-ray luminosity within R_{500}.

name	R_{ext} arcmin	kT keV	kT_{corr} keV	$Z/Z_\odot$	$Z_{corr}/Z_\odot$	F_S erg s^{-1} cm^{-2}	$L_{0.5-2keV}$ 10^{44} erg s^{-1}	L_{bol} 10^{44} erg s^{-1}	Cts (0.5-2 keV)	R_{500} kpc	R_{500} arcmin	$L_{0.5-2keV}$ 10^{44} erg s^{-1}	L_{bol} 10^{44} erg s^{-1}
SWXCS J000315-5255.2	1.73	$5.29^{+0.67}_{-0.61}$	$4.99^{+0.64}_{-0.57}$	$0.61^{+0.34}_{-0.26}$	$0.52^{+0.29}_{-0.22}$	2.93e-14	0.381	1.235	1487.5	820 ± 103	1.99 ± 0.25	$1.78^{+0.70}_{-0.83}$	$5.78^{+2.27}_{-2.68}$
SWXCS J000324-5253.8	2.05	$5.60^{+0.69}_{-0.53}$	$5.41^{+0.66}_{-0.51}$	$0.54^{+0.25}_{-0.21}$	$0.49^{+0.23}_{-0.19}$	4.49e-14	0.921	3.053	1847.4	789 ± 90	1.76 ± 0.20	$3.01^{+0.60}_{-0.64}$	$9.97^{+1.98}_{-2.12}$
SWXCS J002437-5803.9	1.69	$1.25^{+0.08}_{-0.09}$	$1.23^{+0.08}_{-0.09}$	$0.44^{+0.22}_{-0.15}$	$0.40^{+0.20}_{-0.14}$	1.01e-13	0.111	0.187	315.3	492 ± 38	2.52 ± 0.19	$0.137^{+0.009}_{-0.009}$	$0.23^{+0.016}_{-0.016}$
SWXCS J005500-3852.4	1.42	$2.12^{+0.74}_{-0.47}$	$1.87^{+0.65}_{-0.41}$	$0.40^{+0.47}_{-0.28}$	-	7.38e-14	0.054	0.114	104.8	623 ± 179	3.67 ± 1.05	$0.264^{+0.134}_{-0.110}$	$0.56^{+0.284}_{-0.233}$
SWXCS J011432-4828.6	1.85	$4.30^{+1.02}_{-0.65}$	$3.70^{+0.88}_{-0.56}$	$1.09^{+0.71}_{-0.49}$	-	1.12e-13	4.247	12.262	158.2	572 ± 113	1.18 ± 0.23	$3.39^{+0.45}_{-0.46}$	$9.80^{+1.29}_{-1.34}$
SWXCS J021705-5014.2	1.73	$8.29^{+0.99}_{-0.96}$	$8.03^{+0.96}_{-0.93}$	$1.34^{+0.43}_{-0.36}$	$1.26^{+0.40}_{-0.34}$	1.37e-13	1.161	4.891	749.9	1115 ± 137	2.94 ± 0.36	$1.48^{+0.09}_{-0.10}$	$6.24^{+0.36}_{-0.42}$
SWXCS J021747-5003.4	1.14	$3.08^{+0.44}_{-0.39}$	$2.92^{+0.41}_{-0.38}$	$0.86^{+0.53}_{-0.37}$	$0.72^{+0.44}_{-0.31}$	5.38e-14	0.062	0.155	207.6	774 ± 108	3.79 ± 0.53	$0.073^{+0.005}_{-0.005}$	$0.180^{+0.013}_{-0.013}$
SWXCS J023924-2505.1	1.49	$4.12^{+0.92}_{-0.64}$	$3.86^{+0.86}_{-0.60}$	$0.86^{+0.71}_{-0.45}$	$0.70^{+0.58}_{-0.37}$	5.68e-14	0.045	0.130	323.4	911 ± 176	5.12 ± 0.99	$0.114^{+0.017}_{-0.017}$	$0.33^{+0.048}_{-0.050}$
SWXCS J035259-0043.7	1.73	$4.22^{+0.26}_{-0.24}$	$4.17^{+0.25}_{-0.24}$	$0.25^{+0.14}_{-0.12}$	$0.25^{+0.13}_{-0.12}$	3.82e-13	1.277	3.668	1461.4	874 ± 60	3.01 ± 0.21	$1.45^{+0.04}_{-0.04}$	$4.18^{+0.13}_{-0.12}$
SWXCS J044144-1115.6	1.42	$5.54^{+1.43}_{-0.78}$	$5.11^{+1.32}_{-0.72}$	$0.50^{+0.54}_{-0.39}$	$0.40^{+0.43}_{-0.31}$	1.08e-13	0.200	0.670	311.5	1013 ± 205	4.16 ± 0.84	$0.602^{+0.123}_{-0.128}$	$2.02^{+0.41}_{-0.43}$
SWXCS J062155-6228.6	0.51	$3.88^{+0.53}_{-0.62}$	$3.69^{+0.51}_{-0.59}$	$0.86^{+0.50}_{-0.37}$	$0.73^{+0.43}_{-0.32}$	7.66e-15	0.029	0.081	286.9	811 ± 125	2.69 ± 0.41	$0.050^{+0.004}_{-0.004}$	$0.139^{+0.010}_{-0.010}$
SWXCS J082113+3200.1	1.38	$7.58^{+1.27}_{-0.91}$	$7.28^{+1.22}_{-0.87}$	$0.19^{+0.23}_{-0.19}$	$0.18^{+0.21}_{-0.18}$	1.27e-13	1.964	7.494	597.0	966 ± 143	2.25 ± 0.33	$2.31^{+0.13}_{-0.14}$	$8.83^{+0.50}_{-0.55}$
SWXCS J084749+1331.7	2.12	$6.91^{+0.36}_{-0.35}$	$6.83^{+0.35}_{-0.34}$	$0.53^{+0.12}_{-0.11}$	$0.53^{+0.12}_{-0.11}$	1.18e-12	4.152	15.537	3824.0	1126 ± 70	3.78 ± 0.23	$4.65^{+0.09}_{-0.09}$	$17.39^{+0.33}_{-0.34}$
SWXCS J085524+1102.0	1.30	$5.65^{+1.72}_{-1.08}$	$4.79^{+1.46}_{-0.92}$	$0.72^{+0.73}_{-0.50}$	-	5.48e-14	0.222	0.756	204.1	923 ± 231	2.98 ± 0.74	$0.544^{+0.147}_{-0.144}$	$1.85^{+0.50}_{-0.49}$
SWXCS J090946+4157.2	1.81	$1.69^{+0.28}_{-0.21}$	$1.54^{+0.26}_{-0.19}$	$0.66^{+0.53}_{-0.32}$	-	2.45e-13	0.126	0.238	133.5	569 ± 86	3.82 ± 0.58	$0.140^{+0.012}_{-0.013}$	$0.265^{+0.023}_{-0.024}$
SWXCS J092729+3010.8	1.34	$3.34^{+0.28}_{-0.25}$	$3.28^{+0.27}_{-0.25}$	$0.39^{+0.25}_{-0.20}$	$0.38^{+0.24}_{-0.20}$	1.62e-13	0.669	1.719	692.7	757 ± 66	2.46 ± 0.21	$0.787^{+0.033}_{-0.035}$	$2.02^{+0.08}_{-0.09}$
SWXCS J092650+3013.8	0.90	$4.07^{+0.60}_{-0.55}$	$3.77^{+0.55}_{-0.51}$	$0.65^{+0.45}_{-0.32}$	$0.51^{+0.35}_{-0.26}$	4.05e-14	0.473	1.336	254.8	722 ± 105	1.81 ± 0.26	$0.592^{+0.043}_{-0.044}$	$1.67^{+0.12}_{-0.13}$
SWXCS J092719+3013.7	1.10	$3.01^{+0.42}_{-0.36}$	$2.90^{+0.40}_{-0.35}$	$0.46^{+0.39}_{-0.28}$	$0.41^{+0.35}_{-0.25}$	5.41e-14	0.144	0.355	312.1	735 ± 99	2.73 ± 0.37	$0.299^{+0.037}_{-0.035}$	$0.736^{+0.091}_{-0.085}$
SWXCS J093045+1659.5	1.53	$3.25^{+0.98}_{-0.74}$	$2.92^{+0.88}_{-0.67}$	$0.16^{+0.47}_{-0.15}$	-	4.38e-14	0.037	0.094	160.5	786 ± 210	4.34 ± 1.16	$0.161^{+0.070}_{-0.060}$	$0.412^{+0.179}_{-0.153}$
SWXCS J093749+1535.7	0.83	$1.60^{+0.17}_{-0.23}$	$1.41^{+0.15}_{-0.20}$	$1.36^{+1.80}_{-0.77}$	-	3.13e-14	0.068	0.115	107.5	509 ± 66	2.03 ± 0.27	$0.083^{+0.008}_{-0.008}$	$0.140^{+0.014}_{-0.014}$
SWXCS J094816-1316.7	1.14	$0.78^{+0.05}_{-0.05}$	$0.77^{+0.05}_{-0.05}$	$0.24^{+0.13}_{-0.08}$	$0.22^{+0.12}_{-0.07}$	4.26e-14	0.019	0.031	279.7	398 ± 28	2.87 ± 0.20	$0.027^{+0.002}_{-0.002}$	$0.044^{+0.003}_{-0.003}$
SWXCS J101341+4306.9	0.90	$6.85^{+2.03}_{-1.37}$	$5.53^{+1.64}_{-1.10}$	$0.56^{+0.63}_{-0.43}$	-	3.11e-14	0.191	0.712	170.5	953 ± 238	2.73 ± 0.68	$0.782^{+0.250}_{-0.227}$	$2.91^{+0.93}_{-0.84}$
SWXCS J105946+5348.2	2.12	$2.05^{+0.30}_{-0.31}$	$1.90^{+0.28}_{-0.29}$	$0.75^{+0.53}_{-0.34}$	-	2.11e-13	0.026	0.054	177.7	657 ± 101	7.94 ± 1.22	$0.188^{+0.048}_{-0.046}$	$0.387^{+0.100}_{-0.094}$
SWXCS J115811+4529.1	1.30	$5.29^{+1.44}_{-0.99}$	$4.52^{+1.23}_{-0.85}$	$0.81^{+0.74}_{-0.49}$	-	4.10e-14	0.201	0.664	183.7	879 ± 204	2.69 ± 0.62	$0.321^{+0.045}_{-0.049}$	$1.06^{+0.15}_{-0.16}$
SWXCS J123620+2859.1	1.50	$4.61^{+1.52}_{-1.05}$	$3.78^{+1.24}_{-0.86}$	< 0.36	-	1.02e-13	0.146	0.437	140.1	877 ± 246	3.97 ± 1.11	$0.390^{+0.096}_{-0.103}$	$1.17^{+0.31}_{-0.31}$
SWXCS J124312+1704.9	0.83	$3.49^{+1.08}_{-0.69}$	$2.94^{+0.91}_{-0.58}$	< 0.61	-	3.71e-14	0.019	0.051	127.5	802 ± 206	5.31 ± 1.36	$0.113^{+0.026}_{-0.027}$	$0.298^{+0.068}_{-0.071}$
SWXCS J131300+0803.0	1.14	$9.04^{+3.20}_{-2.08}$	$7.36^{+2.61}_{-1.69}$	$0.01^{+0.44}_{-0.01}$	< 0.277	7.54e-14	0.741	3.068	209.8	1041 ± 306	2.65 ± 0.78	$1.37^{+0.24}_{-0.28}$	$5.68^{+1.00}_{-1.14}$
SWXCS J133055+4200.3	1.85	$0.71^{+0.03}_{-0.02}$	$0.71^{+0.03}_{-0.02}$	$1.46^{+1.46}_{-0.76}$	$1.44^{+1.44}_{-0.76}$	8.20e-14	0.007	0.010	755.7	392 ± 19	5.50 ± 0.26	$0.011^{+0.001}_{-0.001}$	$0.015^{+0.001}_{-0.001}$
SWXCS J140637+2743.8	1.85	$9.79^{+1.48}_{-1.10}$	$9.49^{+1.43}_{-1.06}$	$0.76^{+0.32}_{-0.27}$	$0.72^{+0.30}_{-0.26}$	2.90e-13	3.167	14.151	935.4	1171 ± 159	2.91 ± 0.40	$3.57^{+0.16}_{-0.17}$	$15.93^{+0.69}_{-0.78}$
SWXCS J140639+2735.8	1.85	$4.33^{+0.61}_{-0.51}$	$4.19^{+0.59}_{-0.50}$	$0.46^{+0.37}_{-0.28}$	$0.42^{+0.34}_{-0.26}$	1.66e-13	0.269	0.795	458.0	919 ± 124	3.97 ± 0.53	$0.480^{+0.052}_{-0.053}$	$1.42^{+0.15}_{-0.16}$
SWXCS J140728+2749.3	2.12	$5.02^{+0.91}_{-0.93}$	$4.66^{+0.85}_{-0.87}$	$1.60^{+1.03}_{-0.73}$	$1.29^{+0.83}_{-0.59}$	1.08e-13	0.083	0.273	324.9	1009 ± 189	5.69 ± 1.06	$0.199^{+0.035}_{-0.035}$	$0.653^{+0.116}_{-0.116}$
SWXCS J143646+2752.0	0.75	$1.61^{+0.57}_{-0.46}$	$1.45^{+0.51}_{-0.42}$	$0.12^{+0.26}_{-0.12}$	-	1.31e-14	0.028	0.057	134.4	518 ± 167	2.10 ± 0.68	$0.081^{+0.029}_{-0.027}$	$0.161^{+0.057}_{-0.054}$
SWXCS J151324+3057.6	0.55	$2.60^{+0.66}_{-0.51}$	$2.34^{+0.59}_{-0.46}$	< 0.04	-	1.08e-14	0.001	0.003	116.6	734 ± 166	8.91 ± 2.02	$0.029^{+0.007}_{-0.007}$	$0.069^{+0.017}_{-0.017}$
SWXCS J155742+3530.4	2.12	$8.22^{+0.35}_{-0.34}$	$8.12^{+0.34}_{-0.34}$	$0.34^{+0.08}_{-0.07}$	$0.35^{+0.08}_{-0.07}$	1.87e-12	1.194	4.840	11320.4	1362 ± 74	8.23 ± 0.45	$2.19^{+0.05}_{-0.05}$	$8.89^{+0.19}_{-0.21}$
SWXCS J173721+4618.6	1.46	$4.16^{+0.56}_{-0.52}$	$4.04^{+0.54}_{-0.51}$	$0.43^{+0.37}_{-0.30}$	$0.39^{+0.34}_{-0.28}$	8.80e-14	0.116	0.334	475.3	913 ± 122	4.25 ± 0.57	$0.227^{+0.019}_{-0.020}$	$0.655^{+0.056}_{-0.057}$
SWXCS J175640+3329.5	1.26	$1.00^{+0.09}_{-0.10}$	$0.95^{+0.09}_{-0.09}$	$0.13^{+0.10}_{-0.06}$	-	1.04e-13	0.119	0.214	138.2	429 ± 43	2.19 ± 0.22	$0.135^{+0.012}_{-0.012}$	$0.242^{+0.021}_{-0.021}$
SWXCS J215354+1653.8	1.89	$3.33^{+0.61}_{-0.48}$	$3.18^{+0.58}_{-0.46}$	$0.35^{+0.41}_{-0.29}$	$0.30^{+0.36}_{-0.25}$	1.39e-13	0.204	0.528	337.6	800 ± 134	3.60 ± 0.60	$0.513^{+0.124}_{-0.111}$	$1.323^{+0.32}_{-0.289}$
SWXCS J222600-5712.8	2.12	$6.06^{+1.15}_{-0.80}$	$5.68^{+1.08}_{-0.75}$	$1.36^{+0.80}_{-0.57}$	$1.15^{+0.68}_{-0.49}$	3.00e-13	0.125	0.458	398.2	1144 ± 189	8.17 ± 1.35	$0.434^{+0.065}_{-0.065}$	$1.59^{+0.24}_{-0.24}$
SWXCS J222917-1101.1	0.79	$1.31^{+0.10}_{-0.09}$	$1.27^{+0.09}_{-0.09}$	$0.29^{+0.16}_{-0.11}$	-	3.20e-14	0.037	0.067	216.3	499 ± 39	2.50 ± 0.20	$0.040^{+0.003}_{-0.003}$	$0.072^{+0.005}_{-0.005}$
SWXCS J222953+1943.9	2.05	$4.84^{+0.65}_{-0.56}$	$4.73^{+0.64}_{-0.55}$	$0.68^{+0.37}_{-0.28}$	$0.65^{+0.35}_{-0.27}$	1.20e-13	0.189	0.597	679.7	982 ± 128	4.28 ± 0.56	$0.200^{+0.008}_{-0.008}$	$0.632^{+0.025}_{-0.025}$
SWXCS J224207+2333.9	1.53	$9.74^{+3.36}_{-2.43}$	$7.86^{+2.71}_{-1.96}$	< 0.35	< 0.22	1.18e-13	1.950	8.322	237.8	989 ± 296	2.26 ± 0.68	$2.26^{+0.20}_{-0.25}$	$9.63^{+0.87}_{-1.07}$
SWXCS J230754-6815.1	0.90	$0.77^{+0.05}_{-0.09}$	$0.74^{+0.05}_{-0.09}$	$0.28^{+0.25}_{-0.11}$	-	4.40e-14	0.011	0.017	147.1	396 ± 38	3.63 ± 0.35	$0.015^{+0.001}_{-0.001}$	$0.024^{+0.002}_{-0.002}$
SWXCS J232248+0548.2	1.53	$3.58^{+0.30}_{-0.16}$	$3.54^{+0.30}_{-0.16}$	$0.60^{+0.19}_{-0.17}$	$0.60^{+0.19}_{-0.17}$	2.01e-13	0.452	1.212	1549.4	825 ± 61	3.21 ± 0.24	$0.510^{+0.014}_{-0.014}$	$1.37^{+0.03}_{-0.04}$

Table 2. continued.

name	R_{ext} arcmin	kT keV	kT_{corr} keV	$Z/Z_{\odot}$	$Z_{corr}/Z_{\odot}$	F_S erg s^{-1} cm^{-2}	$L_{0.5-2keV}$ 10^{44} erg s^{-1}	L_{bol} 10^{44} erg s^{-1}	Cts (0.5-2 keV)	R_{500} kpc	R_{500} arcmin	$L_{0.5-2keV}$ 10^{44} erg s^{-1}	L_{bol} 10^{44} erg s^{-1}
SWXCS J232345-3130.8	1.34	$5.79^{+0.99}_{-0.77}$	$5.30^{+0.91}_{-0.70}$	$0.38^{+0.33}_{-0.25}$	$0.30^{+0.26}_{-0.20}$	7.35e-14	1.961	6.554	338.0	740 ± 116	1.59 ± 0.25	$2.09^{+0.14}_{-0.15}$	$6.99^{+0.45}_{-0.50}$
SWXCS J233518-6621.7	1.18	$4.48^{+1.17}_{-0.54}$	$4.11^{+1.07}_{-0.49}$	$1.43^{+0.93}_{-0.63}$	$1.10^{+0.71}_{-0.49}$	5.37e-14	0.239	0.731	226.2	844 ± 163	2.66 ± 0.51	$0.395^{+0.051}_{-0.051}$	$1.21^{+0.15}_{-0.16}$
SWXCS J233617-3136.5	2.12	$2.57^{+0.13}_{-0.13}$	$2.54^{+0.13}_{-0.13}$	$0.89^{+0.19}_{-0.16}$	$0.89^{+0.19}_{-0.16}$	7.48e-13	0.069	0.157	1400.1	770 ± 47	10.60 ± 0.65	$0.316^{+0.020}_{-0.019}$	$0.721^{+0.046}_{-0.044}$

Appendix A: Spectral analysis of single sources

In this Section we present the folded spectra for the 46 sources with redshift analyzed in this paper. The best fit has been obtained assuming a single-temperature `mekal` model, as described in the text. Note that the best-fit parameters of the ICM have been obtained by freezing the redshift parameter to the optical value when available, and to the X-ray redshift z_X in the other cases. In the labels we indicate the redshift value used for the X-ray spectral analysis rounded to the third decimal digit or the last significant digit.

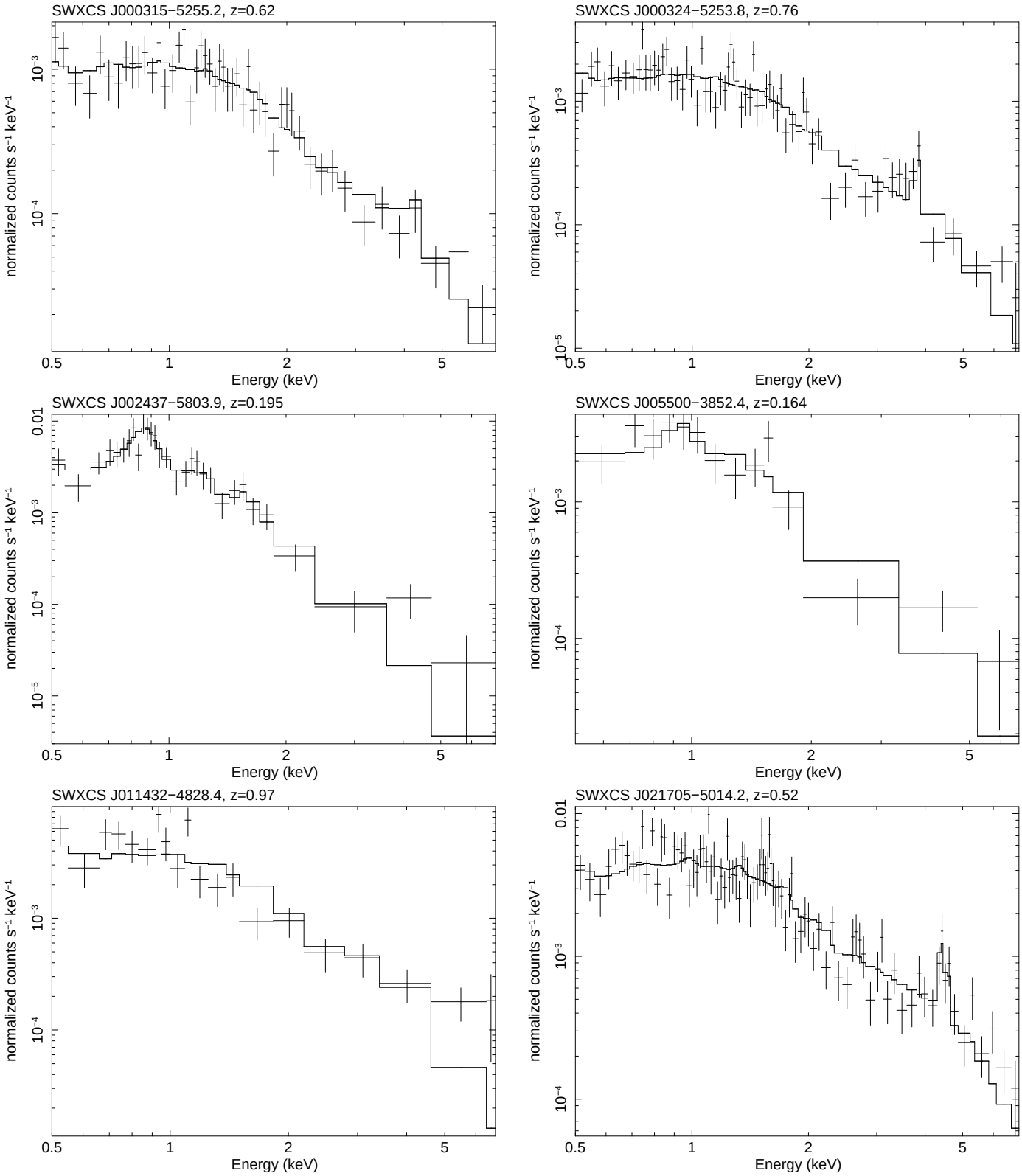

Fig. A.1: Folded spectrum with best-fit model for the 46 sources with redshift analyzed in this paper. The redshift in the label is rounded to the third decimal digit or to the last significant digit.

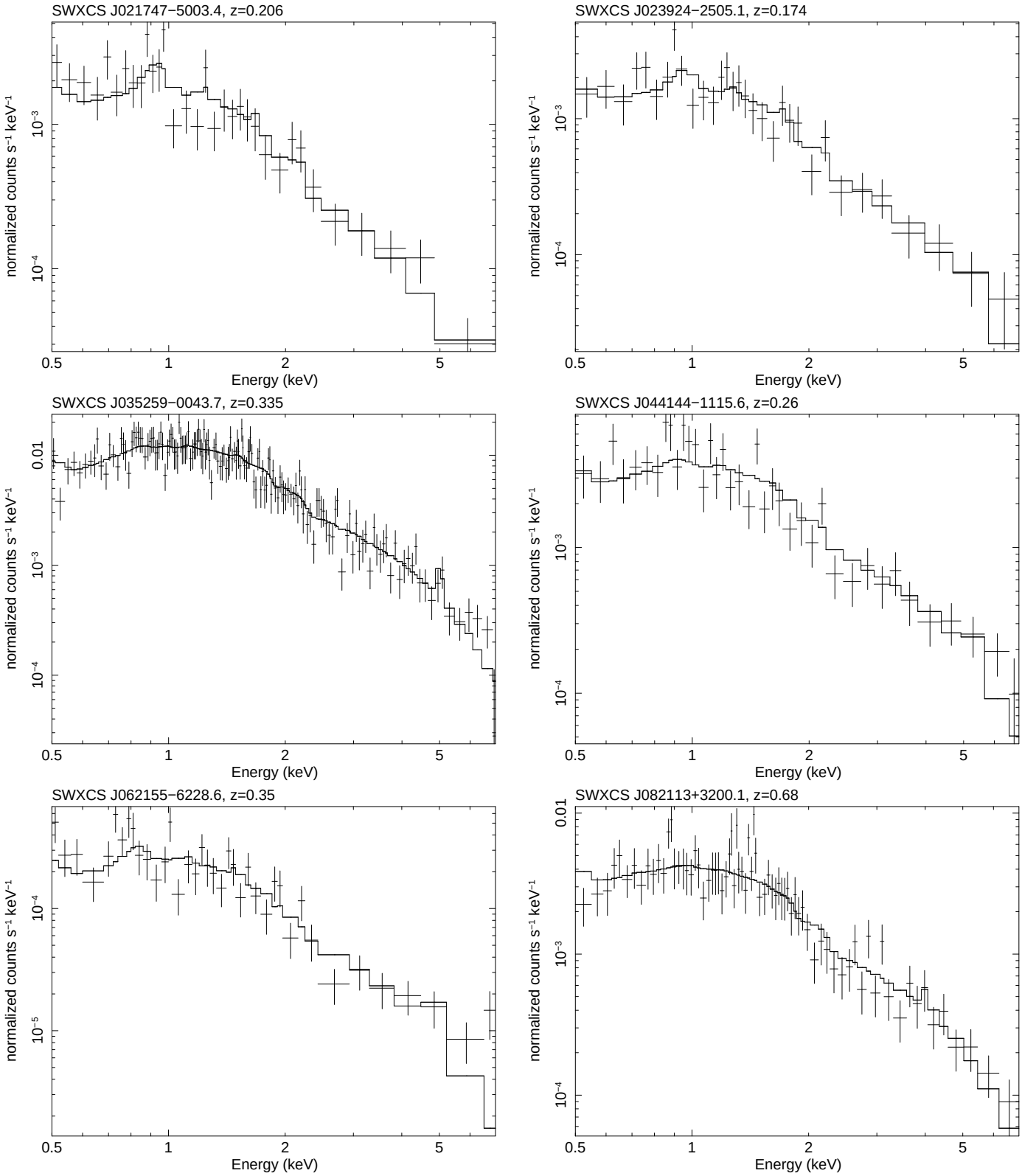

Fig. A.1: continued.

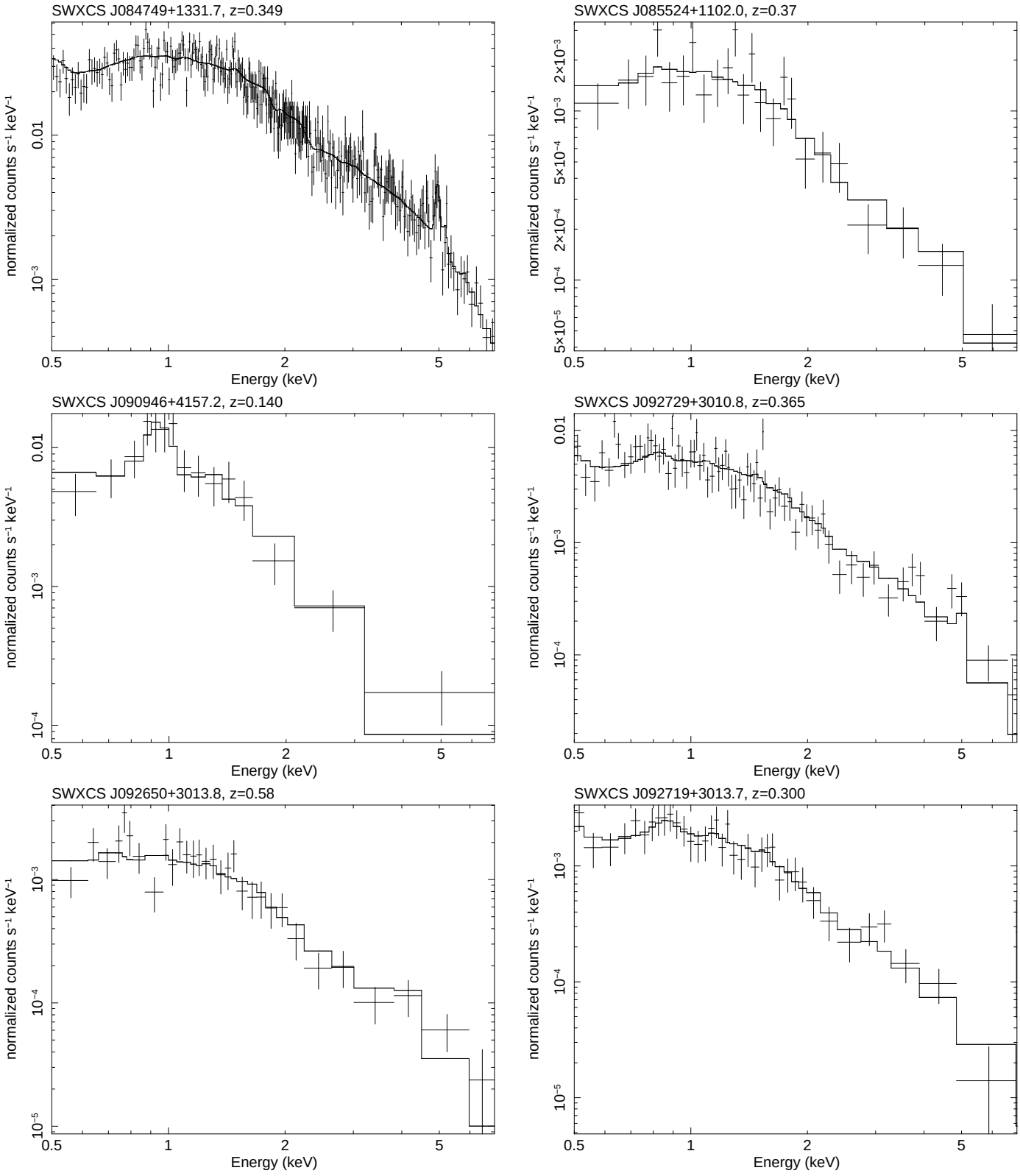

Fig. A.1: continued.

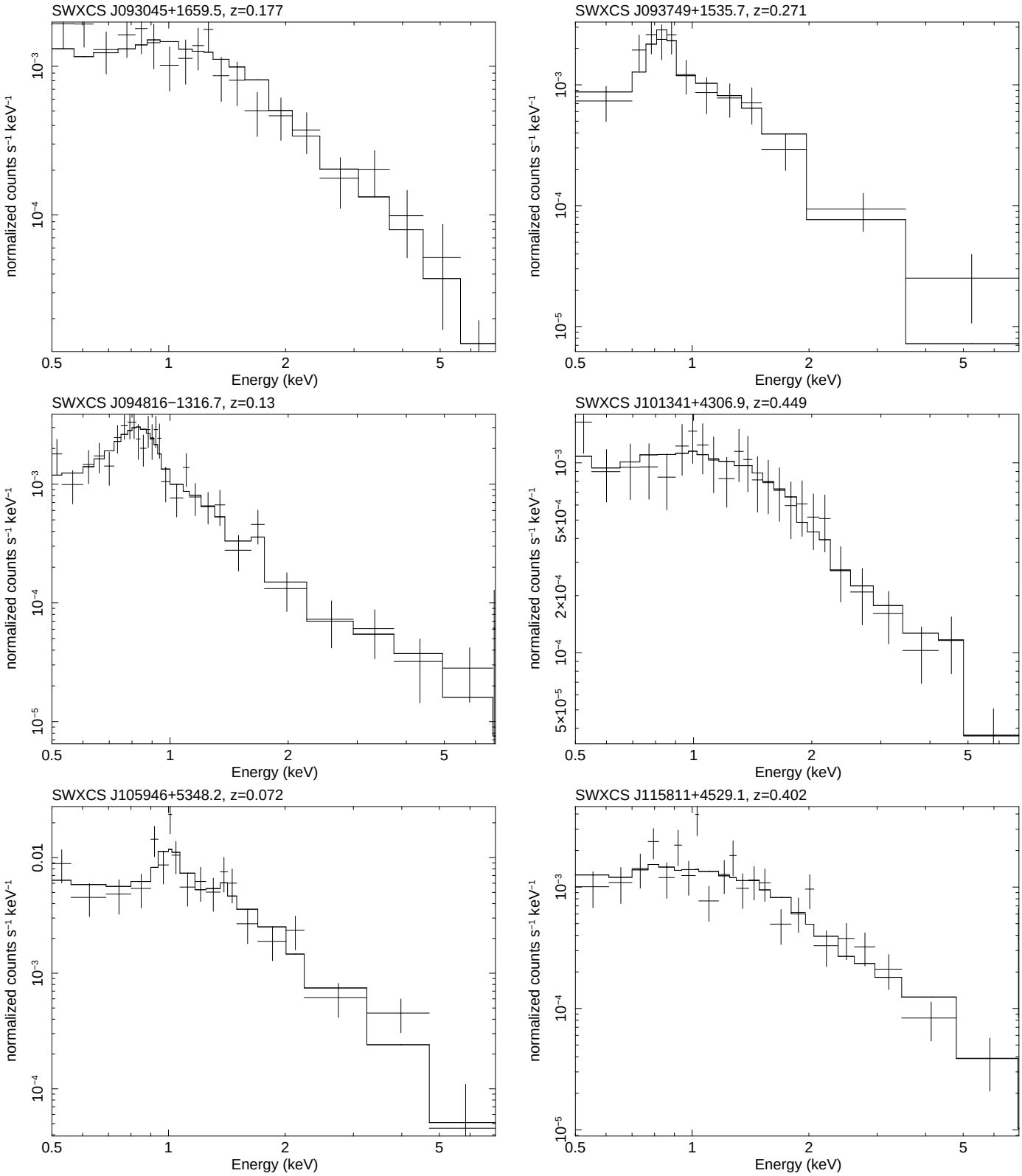

Fig. A.1: continued.

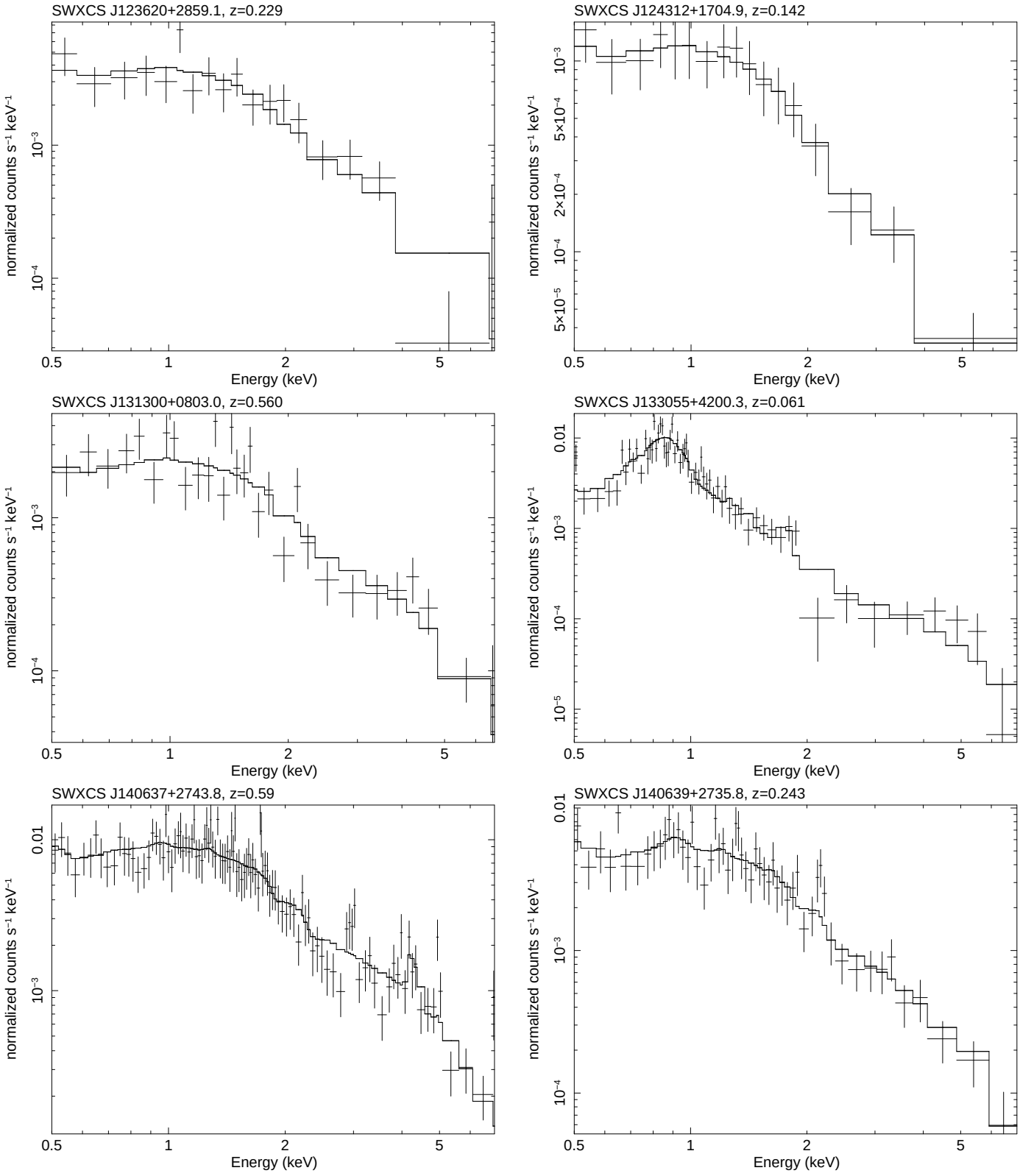

Fig. A.1: continued.

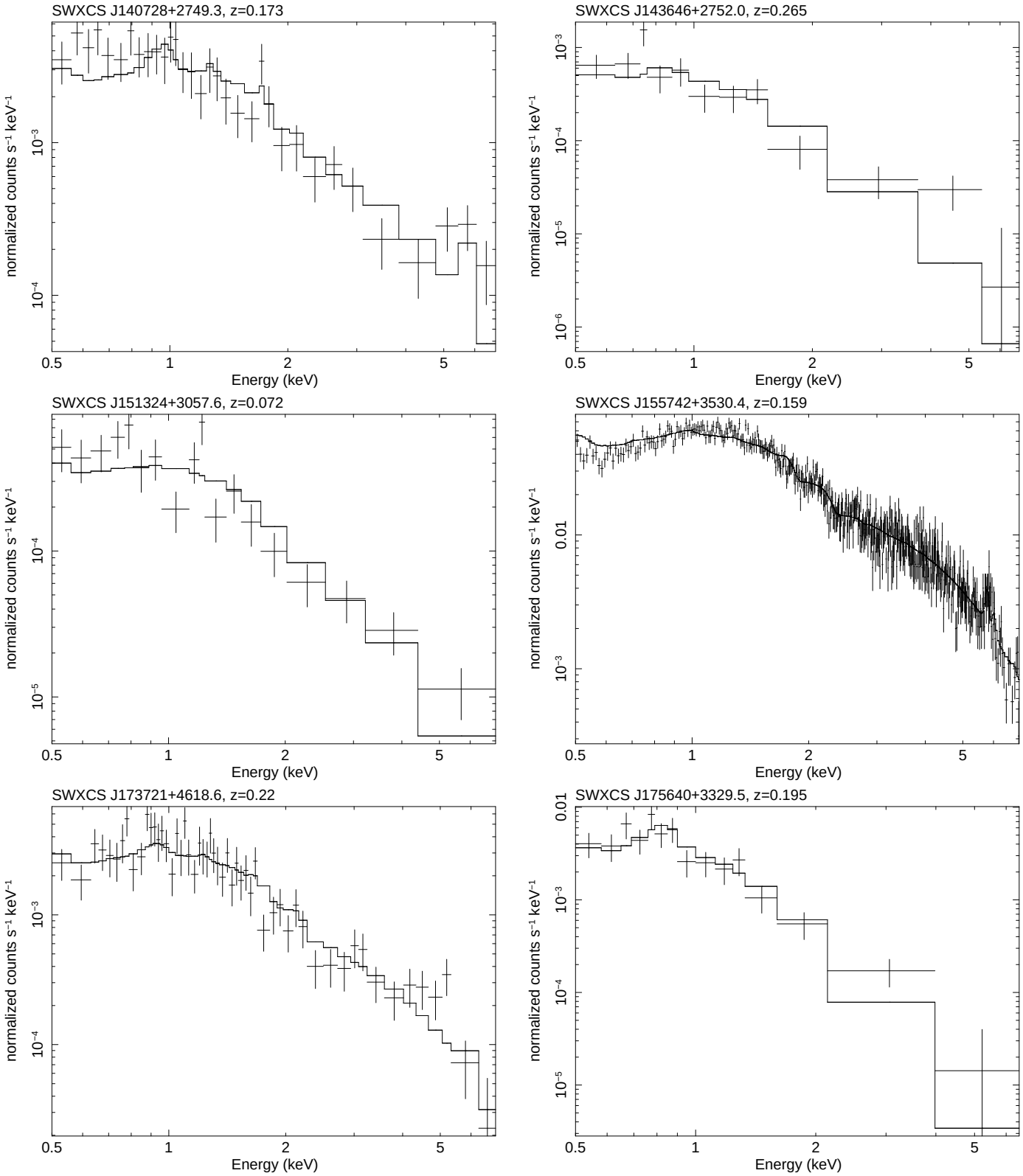

Fig. A.1: continued.

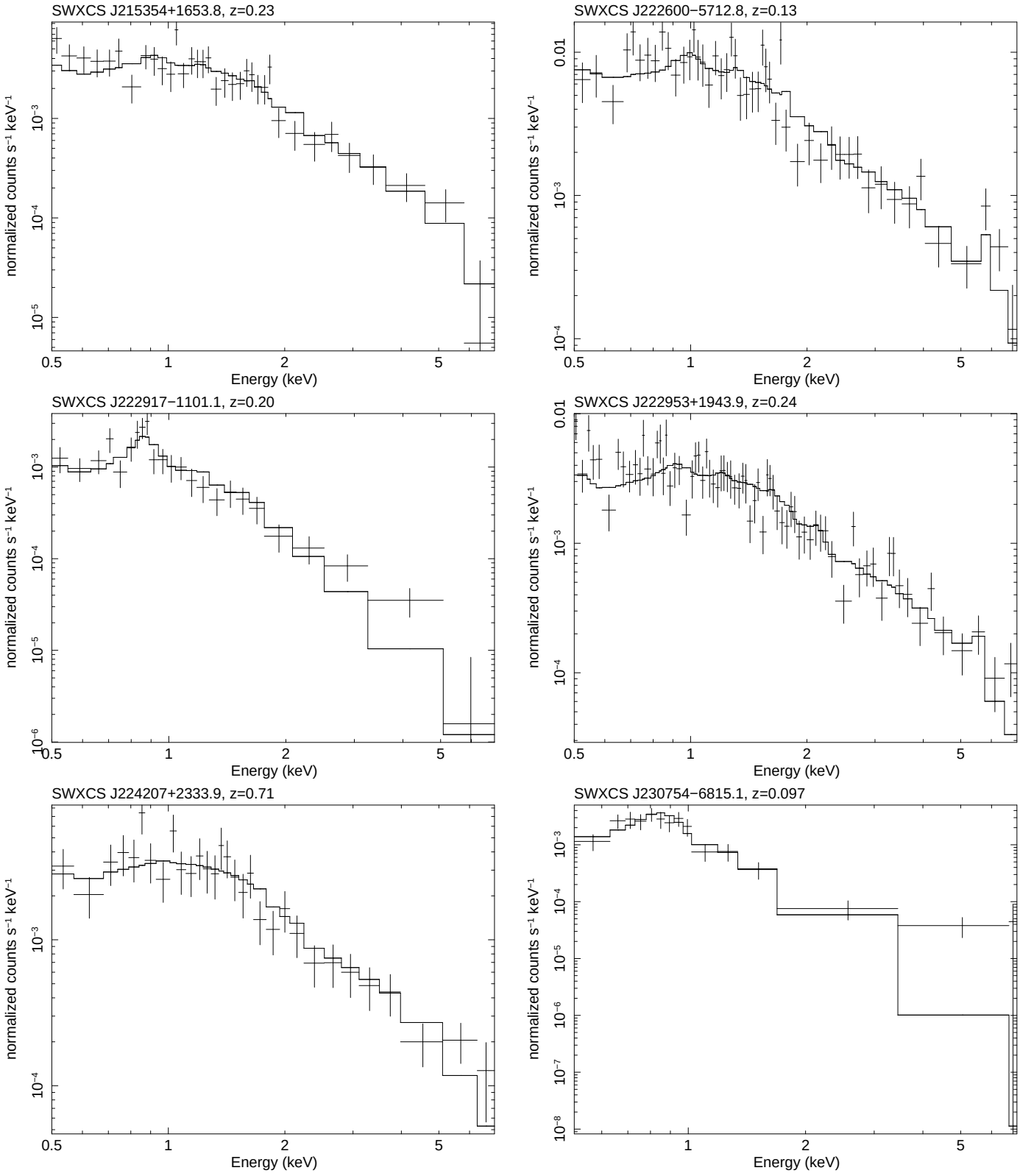

Fig. A.1: continued.

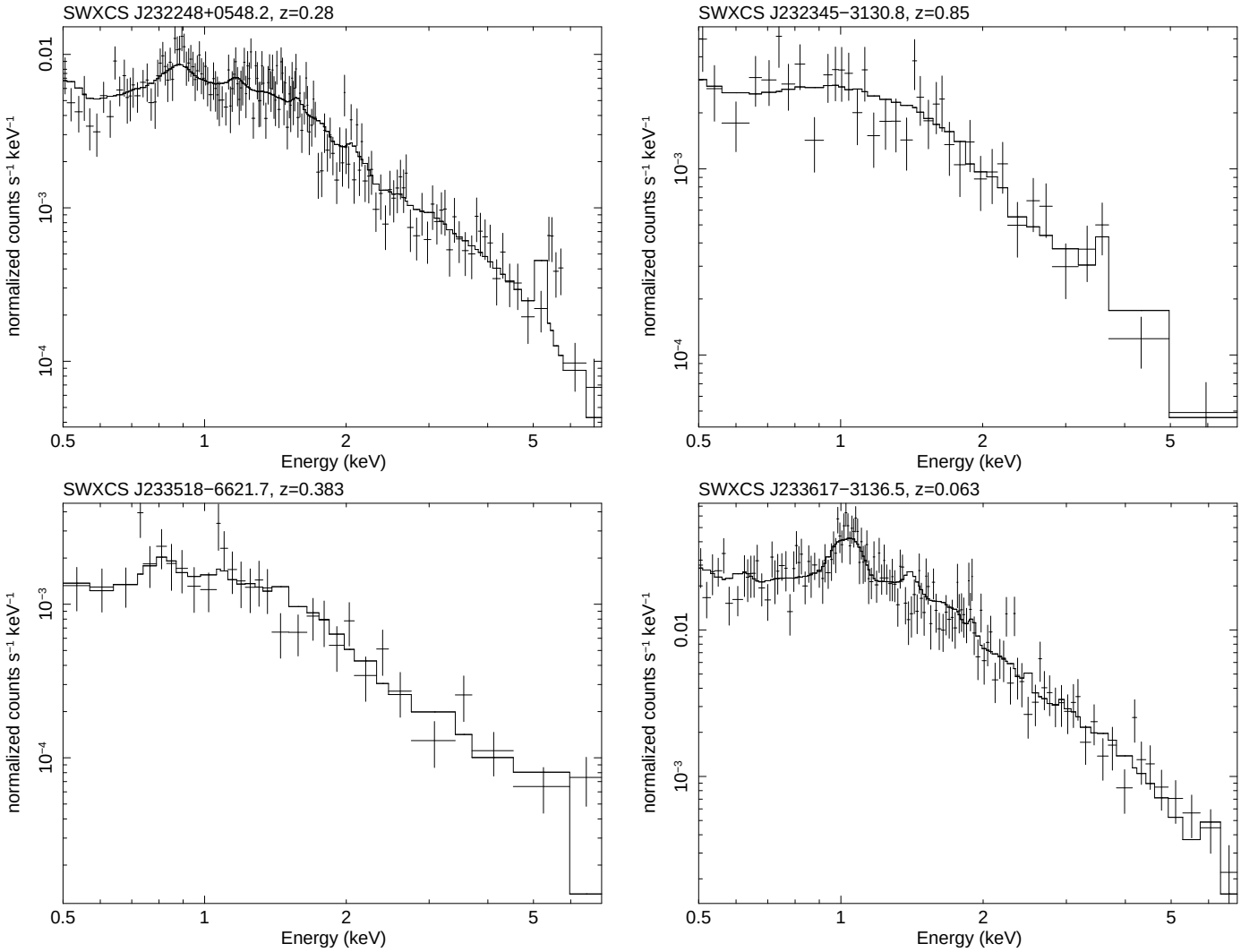

Fig. A.1: continued.

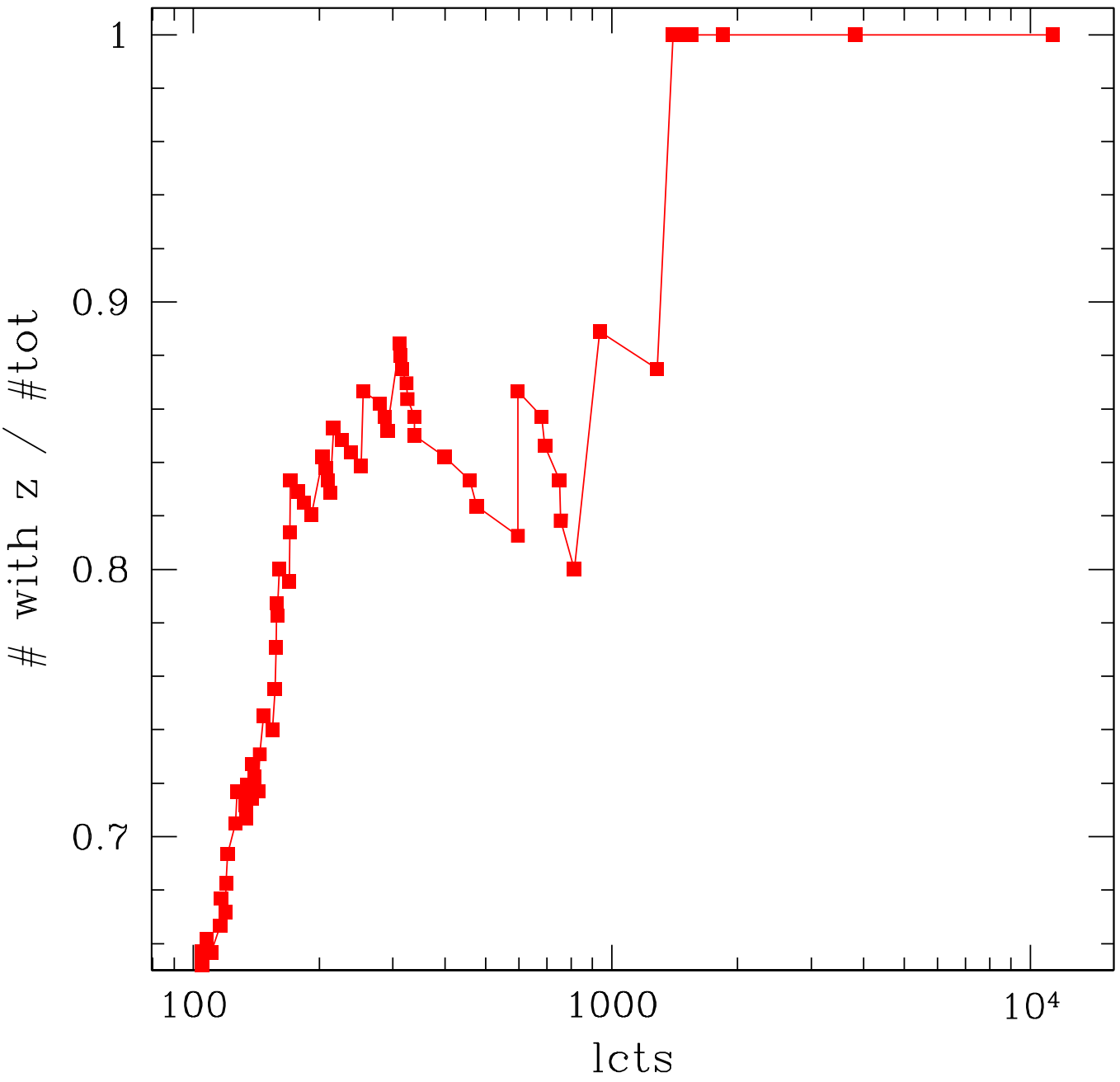
1
0.9
0.8
0.7
with z / #tot
100
1000
10⁴
lcts